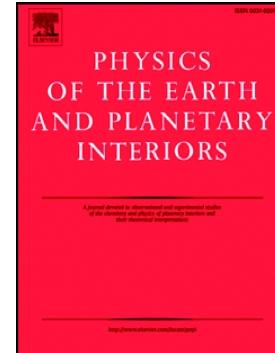


## Journal Pre-proof

Inferring material properties of the lower mantle minerals using Mixture Density Networks

Ashim Rijal, Laura Cobden, Jeannot Trampert, Jennifer M. Jackson, Andrew Valentine



PII: S0031-9201(21)00142-4

DOI: <https://doi.org/10.1016/j.pepi.2021.106784>

Reference: PEPI 106784

To appear in: *Physics of the Earth and Planetary Interiors*

Please cite this article as: A. Rijal, L. Cobden, J. Trampert, et al., Inferring material properties of the lower mantle minerals using Mixture Density Networks, *Physics of the Earth and Planetary Interiors* (2021), <https://doi.org/10.1016/j.pepi.2021.106784>

This is a PDF file of an article that has undergone enhancements after acceptance, such as the addition of a cover page and metadata, and formatting for readability, but it is not yet the definitive version of record. This version will undergo additional copyediting, typesetting and review before it is published in its final form, but we are providing this version to give early visibility of the article. Please note that, during the production process, errors may be discovered which could affect the content, and all legal disclaimers that apply to the journal pertain.

© 2021 The Author(s). Published by Elsevier B.V.

## Highlights

- Equation of state (EOS) modelling is a powerful tool to estimate mineral properties at conditions not accessed by high pressure and temperature experiments.
- Experimental errors, both random and systematic (e.g. pressure scale, functional forms), data consistency and sparsity all contribute to the uncertainties in mineral seismic properties.
- Conventional explicit EOSs which are assumed to follow certain form provide a priori information by fixing their functional form or pressure scale, thereby providing a biased estimate of uncertainties.
- Neural networks based approach can implicitly capture full uncertainties together with highlighting data gaps and identifying data inconsistencies.

# Inferring material properties of the lower mantle minerals using Mixture Density Networks

Ashim Rijal<sup>a,\*</sup>, Laura Cobden<sup>a</sup>, Jeannot Trampert<sup>a</sup>, Jennifer M. Jackson<sup>b</sup>, Andrew Valentine<sup>c</sup>

<sup>a</sup>*Department of Earth Sciences, Utrecht University, Princetonlaan 8a, 3584 CB Utrecht, The Netherlands.*

<sup>b</sup>*Seismological Laboratory, California Institute of Technology, 1200 E. California Blvd., Pasadena, CA 91125, USA.*

<sup>c</sup>*Department of Earth Sciences, Durham University, South Road, Durham, DH1 3LE, UK.*

---

## Abstract

Interpretation of information available from seismic data in terms of temperature and composition requires an understanding of the physical properties of minerals, in particular, the elastic properties of candidate Earth minerals at the relevant (here, lower mantle) pressure and temperature. A common practise for the bulk elastic properties is to measure volume at a range of pressures and temperatures using experiments or computational methods. These datasets are then typically fit to a pre-determined functional form, or equation of state to allow computation of elastic properties at any other pressure or temperature. However, errors, both random and systematic, limitations in the number of data and choice of pressure marker and scale, as well as different functional forms of equations of state, all contribute to the uncertainties in mineral seismic properties. In an attempt to present a more comprehensive view of these uncertainties, we use neural-network based techniques to infer the relationship among: pressure, temperature, volume, bulk modulus, and thermal expansivity of MgO. We illustrate our approach on experimental data, but an extension to ab initio data is straightforward. The type of neural network used is called a Mixture Density Network (MDN) which is a combination of a conventional feed-forward neural network and a mixture

---

\*Corresponding author  
Email address: a.rijal@uu.nl (Ashim Rijal)

model that consists of Gaussian functions. MDNs are capable of approximating arbitrary probability density functions, which allows us to compute the uncertainties in the predicted equations of state. Since the networks interpolate locally between input samples, pressure-volume-temperature relations are implicitly learned from data without imposing any explicit thermodynamic assumptions or ad-hoc relationships. We use the partial derivatives of the mapping between inputs (pressure and temperature) and output (volume) to compute the isothermal bulk modulus and thermal expansivity. Flexibility of the MDNs allows us to investigate the uncertainty due to certain data in one region of pressure-temperature space without influencing the posterior probability density everywhere. In general, we find that the elastic properties of MgO are well-constrained by experimental data. However, our study highlights regions in which sparse or inconsistent data lead to poorly constrained elastic properties, namely: at low pressure and high temperature ( $<25\text{GPa}$  and  $>1500\text{K}$ ), and temperatures above  $2700\text{K}$ . While the former conditions are likely not important for the Earth's lower mantle, they are relevant in other planetary bodies such as the Moon and Mars. Comparison with conventional equation of state forms shows that assuming a certain functional form of the pressure-volume-temperature relationship leads to potential bias in uncertainty quantification, because the uncertainties are then specific to the underlying form. In combination with data sets of other lower mantle minerals, this technique should improve uncertainty quantification in interpretations of seismic data.

*Keywords:* equations of state; lower mantle; neural networks; periclase; MgO

---

## 1. Introduction

Information such as variation of wave speeds (e.g. Dziewonski and Anderson 1981, Kennett et al. 1995), obtained by studying seismic data is crucial for understanding the internal structure of the Earth. Various studies have reported the presence of seismically distinct structures at multiple scales in the Earth's mantle (e.g. Garnero and Helmberger 1998, Ritsema et al. 1999, Romanowicz 2008, Hernlund and Houser 2008, Deschamps et al. 2012,

7 Garnero et al. 2016). In order to relate those observed seismic structures to appropriate  
8 temperature and composition, constraints from mineral physics on the sensitivity of seismic  
9 wave speeds to these parameters are required (e.g. Jackson 1998, Trampert et al. 2001).  
10 The sensitivities have been used to infer the probable existence of chemical heterogeneities  
11 within the mantle (e.g. Trampert et al. 2004, Dobrosavljevic et al. 2019, Jackson and Thomas  
12 2021). Other studies have tried to constrain the (average) mantle geotherm and composition  
13 by combining seismic data and mineral seismic properties (e.g. Cammarano et al. 2003,  
14 2005a,b, Deschamps and Trampert 2004, Stixrude and Lithgow-Bertelloni 2005, Matas et al.  
15 2007, Cobden et al. 2008, 2009, Simmons et al. 2010, Khan et al. 2009, 2011, 2013). Mantle  
16 convection simulations (e.g. Nakagawa et al. 2009, 2010, 2012, Schuberth et al. 2009, 2012)  
17 have also incorporated mineral properties to illustrate the importance of joint geodynamical-  
18 mineralogical approaches to explain the seismic anomalies in the mantle. Mineral properties  
19 can be derived from experimental or theoretical methods. In particular, information on the  
20 density (or volume  $V$ ), incompressibility and rigidity are required to obtain the seismic wave  
21 speeds in a material. Since it is not practical or feasible yet to perform experiments at each  
22 pressure ( $P$ ) and temperature ( $T$ ) that may exist within the Earth, the convention is to use  
23 equations of state (EOSs) to define the relationship among the thermodynamic variables  $P$ ,  
24  $V$  and  $T$  (e.g. Duffy and Wang, 1998), and hence be able to estimate mineral properties at  
25 the conditions not accessed by experiments.

26 However, a number of uncertainties are associated with this procedure. Experimental mea-  
27 surements contain random and systematic errors. The choice of pressure scale as well as  
28 different functional forms of the EOS (e.g. Vinet EOS, third/fourth order finite strain  
29 equations, also called Birch-Murnaghan EOSs, as well as the choice of Grüneisen models)  
30 all contribute to the uncertainties in mineral seismic properties. As a result, it becomes  
31 challenging to determine realistic uncertainties for the interpretations which relate seismic  
32 observations to temperature and composition.

33 In this study, we present an Artificial Neural Network (ANN) based approach to infer the

34 pressure-volume-temperature (P-V-T) relationship of MgO, with a view to extend the appli-  
35 cation to other major lower mantle minerals. We collate experimental P-V-T data for MgO  
36 together with reported uncertainties, regardless of pressure scale or functional form used.  
37 By applying ANN techniques, P-V-T relationships are implicitly learned from data without  
38 any prior assumption on the functional form (or thermodynamic model) of the relationship.  
39 Specifically, we use Mixture Density Networks to infer material properties and assess their  
40 uncertainties. We compute the partial derivatives of inferred volume with respect to pres-  
41 sure and temperature to extract the bulk modulus and thermal expansivity, respectively.  
42 In order to test the feasibility of this approach, we train the networks only on experimen-  
43 tal data, although a combination of theoretical and experimental data is also possible and  
44 straightforward.

## 45 **2. Equations of state: Uncertainties**

46 Experimental approaches (e.g. Vassiliou and Ahrens 1981, Yoneda 1990, Utsumi et al. 1998,  
47 Duffy and Ahrens 1995, Fei 1999, Sinogeikin and Bass 2000, Sinogeikin et al. 2000, Dewaele  
48 et al. 2000, Speziale et al. 2001, Li et al. 2006, Dorogokupets and Dewaele 2007, Hirose et al.  
49 2008, Murakami et al. 2009, Kono et al. 2010, Dorfman et al. 2012, Ye et al. 2017) have  
50 been used to establish the P-V-T relationship of MgO. Experiments using a diamond anvil  
51 cell (DAC), a multi-anvil press (MAP) and shock compression have provided a huge number  
52 of data covering a wide range of pressure and temperature. Laboratory measurements of  
53 volume are done at a discrete set of pressure and temperature points. To cover the en-  
54 tire pressure and temperature range of lower mantle requires pressure extrapolation and/or  
55 interpolation of the measurements using a thermal equation of state. The most common  
56 procedure (e.g. Matas et al. 2007, Cobden et al. 2009) is to use an isothermal equation of  
57 state with a Mie-Grüneisen model for thermal pressure. In this approach, the total pressure  
58 is considered to be the sum of a static pressure and a quasiharmonic thermal pressure. The  
59 static pressure term describes the pressure-volume relationship at a reference temperature

60 (usually 300 K). Different functional forms, such as third/fourth order finite strain and Vinet,  
61 have been widely used to model isothermal compression curves often leading to different esti-  
62 mates of fitting parameters or ambient mineral properties such as volume ( $V_0$ ), bulk modulus  
63 ( $K_{0T}$ ) and pressure derivative of bulk modulus ( $K'_{0T}$ ) at 0 GPa pressure (e.g. Speziale et al.  
64 2001, Dorogokupets and Dewaele 2007, Tange et al. 2009). To compute temperature effects  
65 (more precisely, thermal pressure) this framework uses a Grüneisen parameter whose volume  
66 dependence is uncertain (Ye et al. 2017). Although anharmonic effects are very small com-  
67 pared to the harmonic contribution to thermal pressure, some authors (e.g. Dorogokupets  
68 and Dewaele 2007) use models to account for this term as well.

69 Additionally, the exact determination of pressure using a reliable pressure scale in static high  
70 pressure and temperature experiments is still a challenging task. The ruby pressure scale of  
71 Forman et al. 1972 used in DAC experiments has been largely calibrated (Liu and Bi 2016)  
72 using both static and dynamic compression data, but still suffers from large experimental  
73 uncertainties. Dynamic shock compression experiments provide an absolute pressure scale.  
74 But the correction for thermal effects can be very uncertain (e.g. Dorfman et al. 2012, Duffy  
75 and Wang 1998), especially at high shock temperatures because the corresponding thermal  
76 contribution also increases. Other widely used pressure scales are gold, platinum and MgO  
77 scales. A recent study by Ye et al. 2017 shows the inter-comparison of those scales up to 140  
78 GPa and 2500 K. They report  $\pm 1$  to 4 GPa (sometimes systematic) differences in pressure  
79 among those pressure scales. Although their study optimized different Au, Pt and MgO  
80 pressure scales to make them agree within  $\pm 1$  GPa, it concludes that the most preferred  
81 form of EOS (and the pressure standard itself) remains uncertain.

82 Measurement errors, lack of an absolute pressure scale, and a variety of functional forms  
83 of EOSs all contribute to the uncertainties in mineral seismic properties. Assuming one  
84 particular EOS or pressure scale has the potential to produce biased uncertainty estimates  
85 that are specific to the underlying functional form. In this study we train neural networks  
86 to learn the implicit relation between pressure and temperature (as inputs) and volume,

87 bulk modulus and thermal expansivity (as outputs). The results are entirely data-driven  
 88 without a priori selection of experiments or a functional form to explain the data. In this  
 89 way, we can infer the relative contributions of data sparsity versus prior conditioning to the  
 90 uncertainties. We can also map the level of certainty of the elastic parameters in pressure-  
 91 temperature space, which can be propagated into seismic interpretation.

### 92 3. The Mixture Density Network (MDN)

#### 93 3.1. Background

94 Conventional neural networks (Hornik et al. 1989) are general function approximators, which  
 95 can be used to infer an (arbitrary nonlinear) relationship (Cybenko 1989) between inputs  
 96 and targets/outputs. However, the conditional average (i.e. the mean value of output  
 97 conditioned on input data) given by such networks only provides limited information about  
 98 that relationship (Bishop 1994). Since experimental P-V-T data contain measurement errors,  
 99 and inferring P-V-T relationship using those data is an inverse problem which can have  
 100 multiple solutions, naturally we seek to treat the problem in a probabilistic framework.  
 101 Hence, instead of having only the average volume output, we want to find the posterior  
 102 probability density function (pdf) for volume. The pdf for volume at a given pressure and  
 103 temperature can be denoted as

$$104 \quad \sigma(V|P, T). \quad (1)$$

105 We can represent a general pdf by combining a conventional feed-forward neural network  
 106 with a Gaussian Mixture Model (GMM), which is then called a Mixture Density Network  
 107 (MDN) (Bishop 1994 and Bishop 1995). The architecture of the MDN used in this study is  
 108 shown in Figure 1, and consists of a two layer feed-forward neural network and a GMM. The  
 109 GMM contains a mixture of a finite number of Gaussian kernels which are then weighted to  
 110 give the posterior pdf. The mean, standard deviation and weight of each Gaussian kernel  
 111 are parameterized by weights and biases of the feed-forward neural network, also known as

112 network parameters ( $\alpha$ ).

113 Application of MDNs in Earth Sciences ranges from inversion of surface wave data for global  
 114 crustal thickness (Meier et al. 2007a,b), temperature and water content variations within  
 115 the transition zone (Meier et al. 2009), inference of Earth’s radial seismic structure (de Wit  
 116 et al. 2013), inversion of free oscillations (de Wit et al. 2014), constraints on lower mantle  
 117 anisotropy (de Wit and Trampert 2015), nonlinear petrophysical inversion (Shahraeeni and  
 118 Curtis 2011), source inversion of strong-motion data (Käuffl et al. 2016b), inferring param-  
 119 eters governing mantle convection (Atkins et al. 2016) to travel-time tomography (Earp and  
 120 Curtis 2020). In our case, based on some experimental P-V  $\Gamma$  data, we seek to approximate  
 121 the true posterior pdf (Equation 1) by a parameterized posterior

$$122 \quad p(V|P, T; \alpha) \approx \sigma(V|P, T). \quad (2)$$

123 In other words, for a given pressure and temperature, the posterior probability density for  
 124 volume is given by the pdf in expression 2 which is parameterized by the weights and biases  
 125 ( $\alpha$ ) of the feed-forward neural network. These parameters are learned during the network  
 126 training process (see Sub-section 3.2). The posterior pdf (Equation 2) can be expressed as  
 127 a linear combination of a fixed number of Gaussian kernels (also see Figure 1) as

$$128 \quad p(V|P, T; \alpha) = \sum_{n=1}^M \pi_n(P, T; \alpha) \phi_n(V|P, T; \alpha) \quad (3)$$

129 where  $M$  denotes the number of kernels used, and  $\pi_n$  are mixing coefficients which satisfy

$$130 \quad \sum_{n=1}^M \pi_n(P, T; \alpha) = 1. \quad (4)$$

131 If the number of Gaussian kernels is  $M$ , then the total number of outputs from the feed-  
 132 forward network is  $K= 3M$  because each kernel is parameterized by its weight ( $\pi_n$ ), mean  
 133 ( $\mu_n$ ) and standard deviation ( $\sigma_n$ ). Equation 4 ensures that the posterior integrates to 1

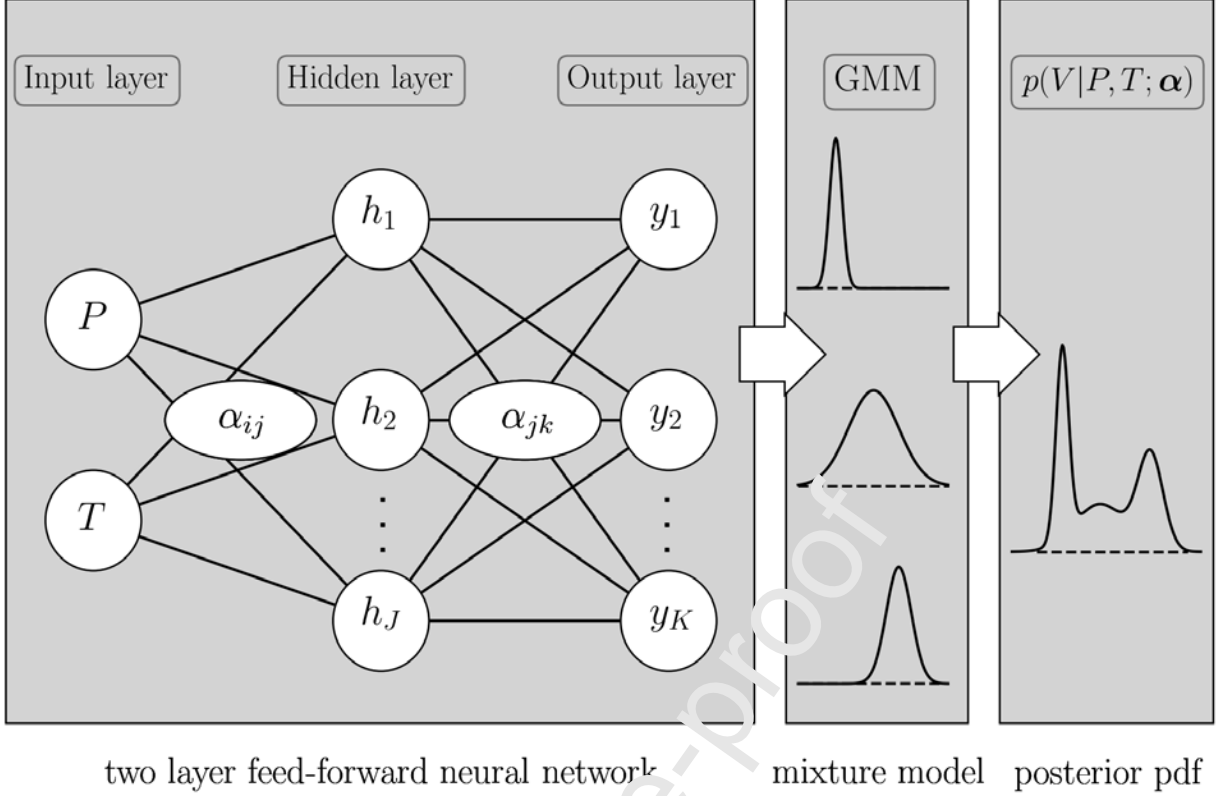


Figure 1: Architecture of the Mixture Density Network (MDN). A two layer feed-forward neural network (left) is combined with a GMM (centre) to get the posterior pdf (right).  $P$  &  $T$  denote the network inputs,  $h_j$  are the hidden nodes, and  $y_k$  are the outputs of the feed-forward network. Indices  $J$  and  $K$  represent the number of hidden and output nodes, respectively. Except for the input nodes, each circle represents a computational node. Hidden layer nodes take a weighted sum (with weights  $\alpha_{ij}$ , where  $i \neq 0$ ) of input data ( $P$  &  $T$ ) plus a bias term ( $\alpha_{0j}$ ) as inputs and apply a sigmoidal activation function. The output layer nodes take a weighted sum (weighted by  $\alpha_{jk}$ , where  $j \neq 0$ ) of the outputs from the hidden layer plus a bias ( $\alpha_{0k}$ ) and apply a linear activation function to give the outputs  $y_k$ . These outputs are related to the mean, standard deviation and weight of each Gaussian in the GMM (see Appendix A for details). Each Gaussian in the GMM is then weighted to give the final posterior pdf.

134 making it a valid probability density.  $\phi_n$  in equation 3 are Gaussian kernels of the form

$$135 \quad \phi_n(V|P, T; \boldsymbol{\alpha}) = \frac{1}{\sqrt{2\pi}\sigma_n(P, T; \boldsymbol{\alpha})} \exp\left\{-\frac{(V - \mu_n(P, T; \boldsymbol{\alpha}))^2}{2\sigma_n(P, T; \boldsymbol{\alpha})^2}\right\} \quad (5)$$

136 where  $\mu_n$  and  $\sigma_n$  are the mean and standard deviation of Gaussian kernels in the GMM.

137 These parameters of the GMM are related to the outputs ( $y_k$ ) of the feed-forward network

138 (see details in Appendix A).

139 *3.2. MDN initialization and training*

140 In order to find the appropriate weights and biases of the feed-forward neural network,  
141 we train the MDN using a sub-set of the experimental P-V-T data. In fact, the total  
142 experimental P-V-T data, shown in Figure 2 (Fei 1999, Jacobsen et al. 2008, Fei et al.  
143 2004a, Fei et al. 2004b, Dewaele et al. 2000, Speziale et al. 2001, Utsumi et al. 1998, Fiquet  
144 et al. 1999, Ye et al. 2017, Kono et al. 2010, Dorfman et al. 2012, Zhang 2000, Fiquet et al.  
145 1996, Dubrovinsky and Saxena 1997, Hirose et al. 2008, Litasov et al. 2005, Murakami et al.  
146 2012, Sinogeikin and Bass 2000, Li et al. 2006 and Fan et al. 2019), is divided into three  
147 sets: training (70%), monitoring (20%) and test (10%) sets. During training, the MDN takes  
148 pressure and temperature from the training data and outputs a pdf for volume according  
149 to Equation 3. However, we need to decide on the initial values of the network parameters  
150 of the feed-forward neural network to compute the first output. We randomly draw the  
151 input layer and hidden layer weights (Bishop 1995) according to Gaussian distributions (see  
152 Appendix B for details). Once the MDN is initialized and training has started, the difference  
153 between the output and the target can be computed according to an error function defined  
154 in Appendix B. This function is also called the loss function which is minimized iteratively  
155 using the ADAM optimization method (see detailed algorithm in Kingma and Ba 2014). We  
156 use TensorFlow (1.13.1) (Abadi et al. 2015) to construct, train and evaluate the MDN.

157 Overfitting is a general property of the maximum likelihood technique (Bishop 1995). We  
158 use a separate monitoring data set to monitor the error decay during training. We evaluate  
159 the monitoring set error at the end of each iteration; if the monitoring error starts to increase  
160 (i.e. the network starts to over-fit the training data) then we stop the training procedure and  
161 save the last best trained model. This technique is also called the early-stopping technique.

162 It is known that the inverse problem can have multiple solutions (i.e. a range of network  
163 parameters can possibly provide equally likely solutions). We train a number of independent  
164 MDNs, and combine them by a weighted sum (e.g. Käuffl et al. 2016a). The weight of each  
165 network is based on how well it performs on the test data which is not used during training.

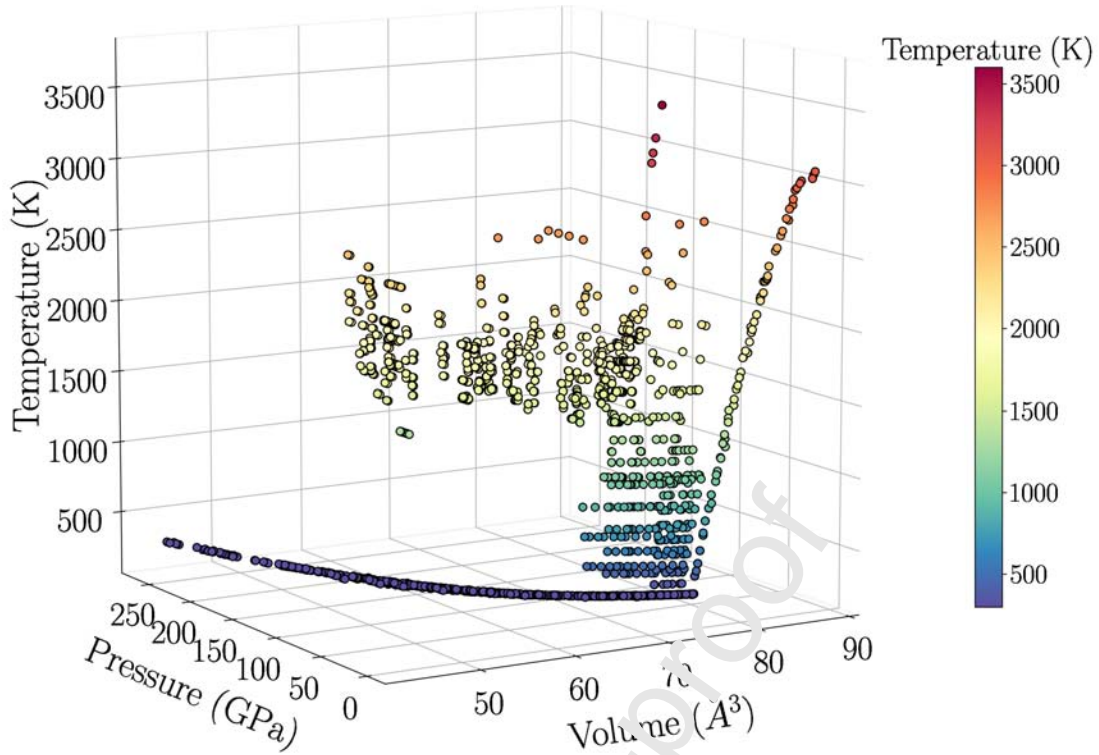


Figure 2: Experimental P-V-T data for MgO used in this study (Fei 1999, Jacobsen et al. 2008, Fei et al. 2004a, Fei et al. 2004b, Dewaele et al. 2000, Speziale et al. 2001, Utsumi et al. 1998, Fiquet et al. 1999, Ye et al. 2017, Kono et al. 2010, Dorfman et al. 2012, Zhang 2000, Fiquet et al. 1996, Dubrovinsky and Saxena 1997, Hirose et al. 2008, Litasov et al. 2005, Morabani et al. 2012, Sinogeikin and Bass 2000, Li et al. 2006 and Fan et al. 2019) to train the MDNs. Data with uncertainties from X-ray diffraction experiments (in static high P-T, Brillouin spectroscopy and ultrasonic interferometry) are collected for the analysis. Note: uncertainties in collected experimental data are not plotted because the scale would be inappropriate to visualize them.

166 The performance is measured by the same error function that we use to calculate training  
 167 and monitoring errors (for details see Appendix B). In this way, the explicit dependence of  
 168 the posterior on the network parameters can be avoided. The choice of the number of MDNs  
 169 depends on the problem at hand. A rough estimate for a relatively simple problem (e.g. a  
 170 few inputs and a target/output) may lie in the range 10-20 (Käuffel et al. 2016a). However,  
 171 in order to compute the uncertainties in bulk modulus and thermal expansivity (details in  
 172 Section 5) we train a large number of MDNs ( $10^3$ ). The number of hidden nodes to use in  
 173 each MDN are randomly selected from a pre-defined range which is 16-32. We conducted a  
 174 separate test (not shown here) to find the range that provides the lowest errors for the test  
 175 set. Similarly, we propagate the uncertainties in experimental data through the MDNs by  
 176 randomly perturbing the thermodynamic variables within the reported uncertainty range.

177 *3.3. Network performance*

178 We use the test data set to examine how well the trained MDNs perform when a new datum  
 179 is presented. Since the test data are not used in network training, we can use them to  
 180 predict the output and subsequently compare with target data. In Figure 3 (top panel) the  
 181 predicted volume is compared with the target data. The MDNs predict pdfs for volume, and  
 182 for this comparison we compute the conditional mean volume (conditioned on inputs P &  
 183 T), instead of using the full posterior pdfs on volume, as

$$184 \quad \langle V|P, T; \boldsymbol{\alpha} \rangle = \sum_{n=1}^M \pi_n(P, T; \boldsymbol{\alpha}) \mu_n(P, T; \boldsymbol{\alpha}). \quad (6)$$

185 This special case of MDN corresponds to the standard neural network output (Bishop 1994),  
 186 i.e. only the feed-forward network with one volume output. Equation 6 shows the mean  
 187 volume output for one MDN, and we calculate the weighted sum (weights are chosen ac-  
 188 cording to the test set error as mentioned previously) of mean volumes from all MDNs. One  
 189 alternative to the conditional posterior mean could be the posterior mode. However, the  
 190 posterior mode may be biased towards certain pressure scales which contain relatively more  
 191 data in the training set compared to other scales.

192 In the region of high temperatures and low pressures (Figure 3, top panel) the trained MDNs  
 193 show lower resolving capacity, providing more uncertain volume predictions. We found that  
 194 this discrepancy in network predictions comes from the inclusion of specific training data  
 195 points (high temperature data of Fiquet et al. 1996) in those ranges. We note that Fiquet  
 196 et al. 1996 did not include a thermal pressure term in their experiments and so it is likely  
 197 that the total pressure is underestimated. Moreover, the reported temperatures are likely  
 198 overestimated by about 20 to 50%. We trained another network excluding these data in our  
 199 training set and assess the prediction performance (Figure 3, bottom panel). In doing so,  
 200 MgO volumes are resolved within the prior range of experimental data, also in the region  
 201 of low pressure and high temperature. This shows the networks' ability to capture the

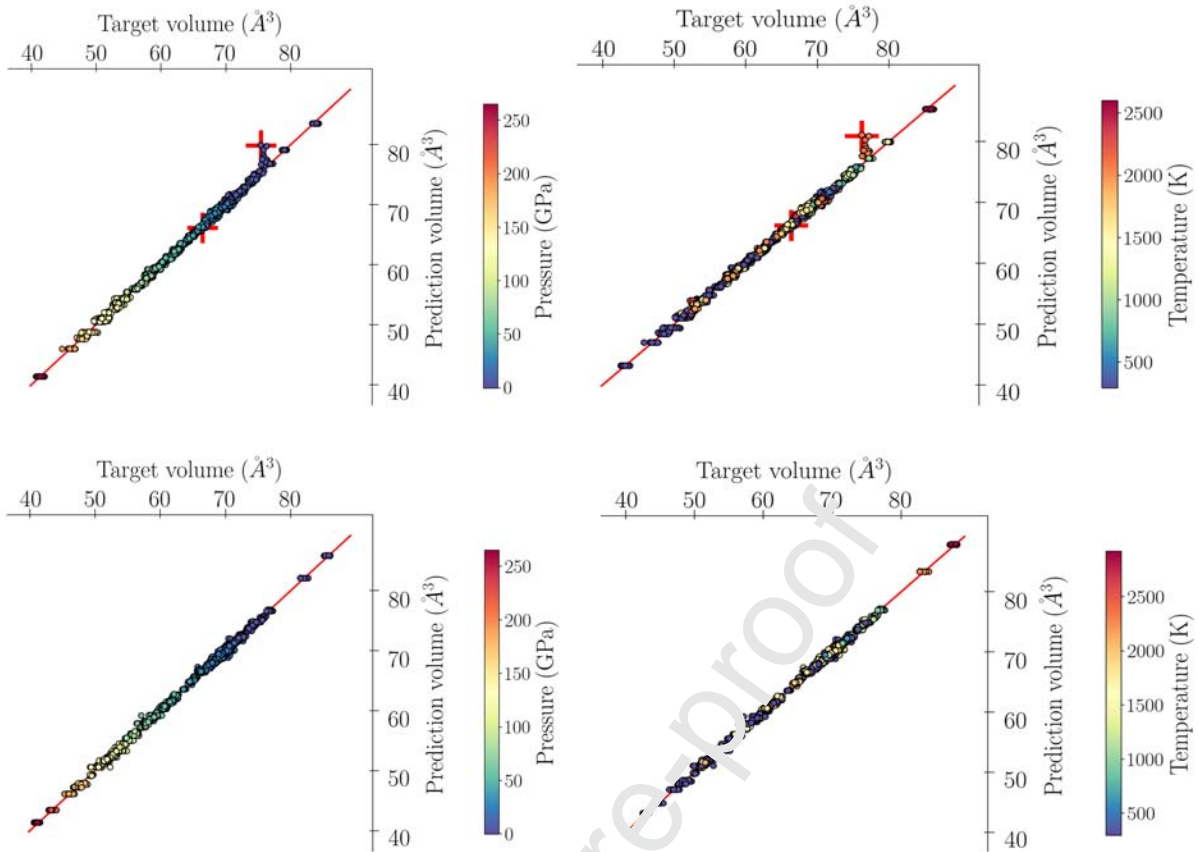


Figure 3: Performance of MDNs. Target volumes from the test data set are compared with mean volumes (Equation 6) predicted by the MDNs. Top panel shows mean volumes predicted by the MDNs trained with all experimental data while bottom shows results with high temperature data of Fiquet et al. 1996 and Murakami et al. 2012 excluded (also see Section 4.2). The pressure (left) and temperature (right) range of the test data set is shown by colourbars on both panels. We note that the solid red line in the Figure refers to a perfectly resolved network prediction. Points located near this line are well resolved and those located away represent more uncertain volume predictions. The MDNs best predict the volumes in low temperature regions and at simultaneous high temperature and pressure. However, including high temperature data of Fiquet et al. 1996 into training provides more uncertain volume predictions in the low pressure, high temperature region. For two data points marked with “+” in both left and right plots in the top panel, we plot posterior pdfs for volume in Figure 4. One datum is located in the low pressure, high temperature region where the effect of high temperature data from Fiquet et al. 1996 is significant and another away from it.

202 underlying data consistency.

203 Low pressure data (approximately less than 30 GPa) are relatively dense up to about 1400 K  
 204 compared to higher temperatures. Similarly, most of the high pressure data, i.e. extending to  
 205 the lower mantle environment, come either from approximately between 1500 K to 2700 K or  
 206 from ambient temperature measurements. Besides that, the experimental data doesn't cover  
 207 simultaneous high temperature and high pressure regions, for example temperatures greater

208 than  $\sim 2700$  K at pressures expected near the bottom of lower mantle. Hence, we expect  
 209 wider posterior probability density functions for volume in regions of sparse experimental  
 210 data coverage.

211 So far we have only shown the mean of the posterior pdf for volume. To illustrate more  
 212 clearly the effect of the high temperature data of Fiquet et al. 1996 on the posterior pdf  
 213 at low pressure, high temperature, we take two data points from the test set (denoted by  
 214 ‘+’ in Figure 3, top panel). Both points are drawn at low pressures, but one is at high  
 215 temperature and located away from the solid line and another at low temperature is close  
 216 to it. In Figure 4 posterior pdfs at those points are shown. They show a more uncertain  
 217 prediction for the high temperature, low pressure input. Once we remove Fiquet et al.  
 218 1996 data from training (see Sub-section 4.2), the network predicts narrow posterior pdfs  
 219 showing less uncertainty (cf. including those in training) in volume. Although excluding  
 220 Fiquet et al. 1996 provides less uncertain volume predictions, due to limited availability of  
 221 experimental data at high temperature and low pressure (approximately  $>1500$  K and  $< 25$   
 222 GPa) the predicted posterior pdfs are still slightly wider than at similar temperatures and  
 223 high pressures (also see Sub-section 4.2 and Appendix C.1).

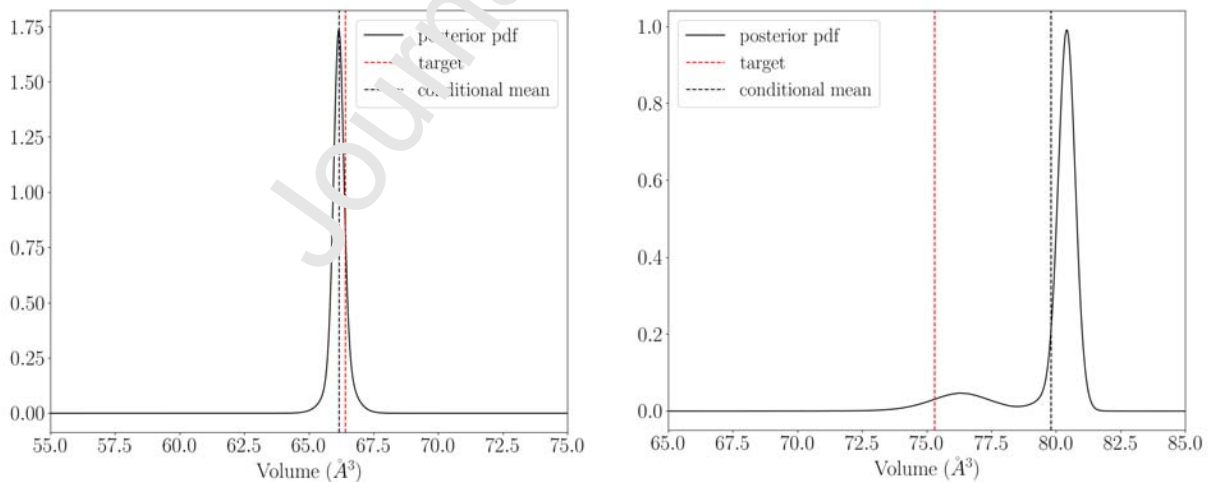


Figure 4: Posterior pdfs for MgO volume (solid curves) for two data points from top panel of Figure 3 together with their target values (red dashed line) and conditional mean volume (black dashed line). Left: inputs are 24.86 GPa and 300.19 K. The posterior pdf is narrow and uni-modal with the posterior mode located close to the target value. Right: inputs are 1.36 GPa and 2116.03 K. The posterior pdf is broad and multi-modal with target volume located away from the posterior modes. The smaller peak is the due to experimental P-V-T data of Fiquet et al. 1996.

## 224 4. MDN predicted material properties

### 225 4.1. $P$ - $V$ relationship at 300 K

226 The predicted pdfs for volume along a 300 K isotherm are presented in Figure 5. A subset of  
 227 the training data (i.e. only around 300 K temperature) is also shown along with the MDN  
 228 predictions. The uncertainty in volume increases with pressure as shown by the increasing  
 229 width of pdfs. This is expected as the training data (around 300 K) are more consistent  
 230 with each other at lower pressures.

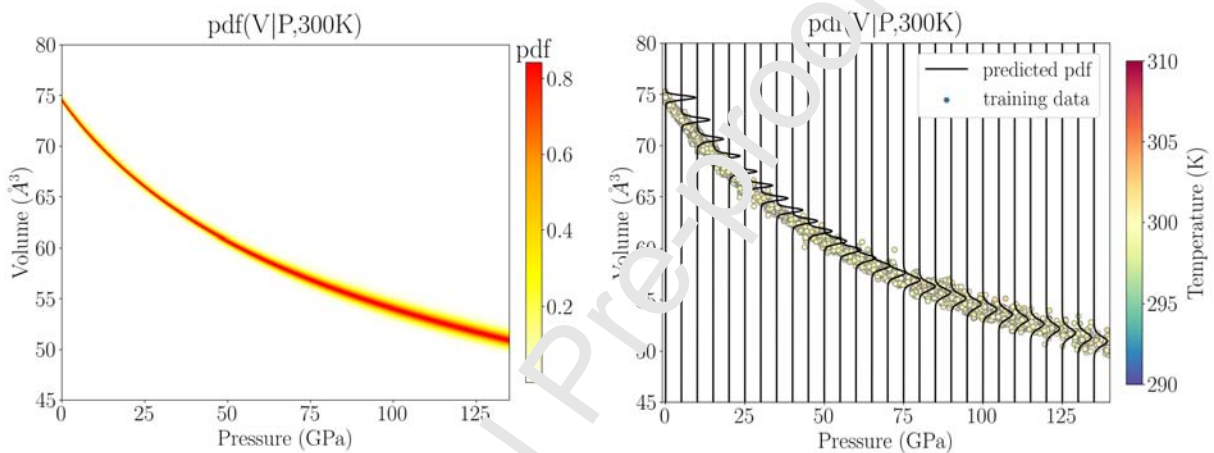


Figure 5: The predicted pdf by the MDNs for volume of MgO along a 300 K isotherm. Left: pdf for volume up to lower mantle pressures is shown as a continuous function of pressure. The colour scale shows the value of the probability density function. Right: pdfs on volume are shown at 5 GPa pressure intervals together with training data around 300 K (shown as circles in the background). The training data show less variation at low pressures which results in narrower pdfs compared to high pressures.

231 In Figure 6 we compare pdfs for the volume of MgO along a 300 K isotherm with EOSs  
 232 of Tange et al. 2009, Speziale et al. 2001, Stixrude and Lithgow-Bertelloni 2005, 2011 and  
 233 Dorogokupets and Dewaele 2007 (denoted as T09, S01, SLB0511 and DD07, respectively). In  
 234 this study, we use MINUTI (Sturhahn 2020) to compute volume, bulk modulus and thermal  
 235 expansivity as a function of pressure (and temperature) from these EOSs. For ambient  
 236 temperature comparisons, static equations (i.e. third-order finite strain or Vinet) together  
 237 with respective fitting parameters ( $V_0$ ,  $K_{0T}$  and  $K'_{0T}$ ) as reported in the literature are used.  
 238 We show the pdfs for volume (Figure 6, left panel) at every 5 GPa. The EOSs diverge as  
 239 the pressure increases. At 135 GPa, the difference in volume between the equations of state

240 of Stixrude and Lithgow-Bertelloni 2005, 2011 and Tange et al. 2009 is  $\sim 0.68 \text{ \AA}^3$ , whereas  
 241 one standard deviation predicted by the neural networks is  $\pm 0.54 \text{ \AA}^3$ . Moreover, the slope of  
 242 each individual EOS differs. This can best be visualized by computing  $\frac{\partial P}{\partial V}$  for all EOSs (see  
 243 Figure 6, right panel). Although Speziale et al. 2001 and Stixrude and Lithgow-Bertelloni  
 244 2005, 2011 are based on third order Birch-Murnaghan EOSs, their fitting parameters are  
 245 different. Comparisons between different EOSs and their fitting parameters are given by  
 246 other studies (e.g. Dorogokupets and Dewaele 2007, Tange et al. 2009, Ye et al. 2017, etc.).  
 247 The mean slope predicted by the neural network shows a slightly stiffer EOS compared to  
 248 the "standard" EOSs from the literature. This may be due to the fact that our training data  
 249 include experiments which make use of different pressure standards (e.g. Ruby, NaCl, Pt,  
 250 Au) than the EOSs considered for comparison (which are based on MgO). Nevertheless, such  
 251 a difference in slope together with the volume difference will inevitably lead to a significant  
 252 divergence in the inferred compressibility and thermal expansivity (see Section 5).

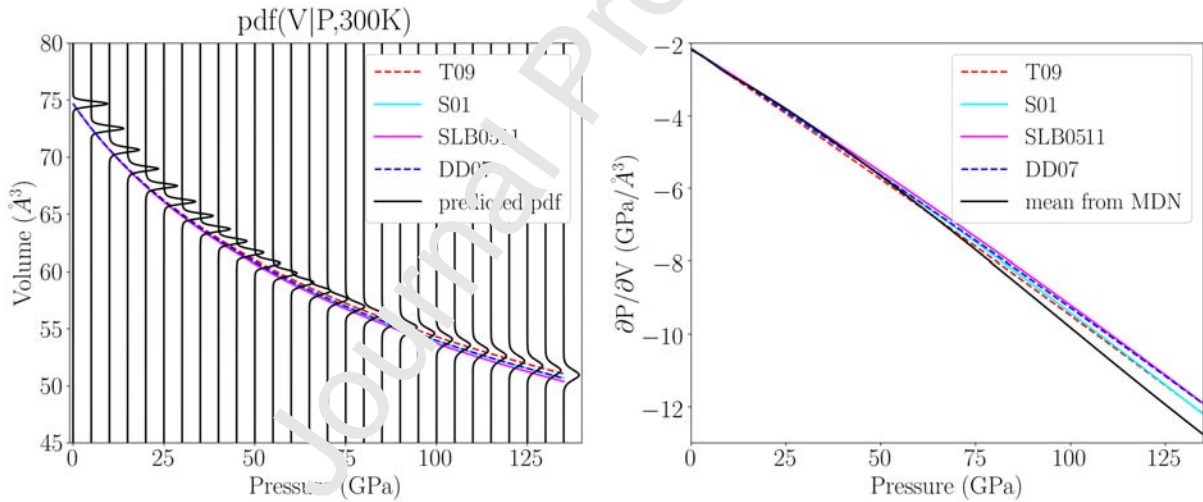


Figure 6: Left: our predicted pdfs for volume of MgO along a 300 K isotherm (black lines) compared with previously published EOSs (Tange et al. 2009, Speziale et al. 2001, Stixrude and Lithgow-Bertelloni 2005, 2011 and Dorogokupets and Dewaele 2007) (coloured lines). Pdfs for volume are shown at 5 GPa pressure intervals. Right:  $\frac{\partial P}{\partial V}$  of MgO EOSs from the left panel. For this computation, we take the mean (Equation 6) of the output posterior on volume at every 0.1 GPa interval. The divergence between different EOSs increases with pressure.

253 *4.2. High temperature P-V-T relationships*

254 We use the trained MDNs to predict volumes of MgO at different temperatures. As an  
255 example, we plot the predicted pdfs for volume along a 2500 K isotherm in Figure 7, left panel  
256 (other isotherms are provided in Appendix C.1). Similar to the ambient temperature (Sub-  
257 section 4.1), the 2500 K isotherm shows a well-constrained volume prediction at lower mantle  
258 pressures. However, the high temperature pdfs show more uncertain volume predictions at  
259 low pressures (except at 0 GPa). For example, at 5 GPa the pdf is relatively wide and  
260 bimodal compared to that at high pressures (e.g. 100 GPa) which is unimodal. As discussed  
261 earlier in Section 3.3, high temperature experimental data of Fiquet et al. 1996 do not include  
262 a thermal pressure term, and it is likely the total pressure is underestimated. This can be  
263 visualised in Figure 7, left panel, where training data points located approximately between  
264 5-15 GPa have a smaller volume compared to data around 20 GPa and  $\sim 2500$  K. We train  
265 another network without the high temperature data of Fiquet et al. 1996 and plot the results  
266 on the right panel of Figure 7. The posterior pdf for volume at 5 GPa now shows a unimodal  
267 peak and the width is decreased by approximately a factor of 2 (cf. left panel at 5 GPa).  
268 Although removing Fiquet et al. 1996 reduces the uncertainties in volume, the posterior pdf  
269 is still wider than at high pressures for the same temperature. This region of low pressure,  
270 high temperature is known to be dominated by anharmonic effects. Although these effects  
271 are implicitly represented in our volume pdfs, there are limited experimental data in this  
272 region (temperature  $>1500$  K and pressure  $<25$  GPa) to further constrain them.

273 We compare the MDN predicted pdfs along a 2500 K isotherm (Figure 7) with some conven-  
274 tional EOSs (Tange et al. 2009, Speziale et al. 2001, Stixrude and Lithgow-Bertelloni 2005,  
275 2011 and Dorogokupets and Dewaele 2007). The variation in volume between these EOSs  
276 at high pressures is similar to that observed at 300 K. It has been noted in earlier studies  
277 (e.g. Ye et al. 2017) that the discrepancies in high temperature EOSs are partly due to  
278 persistence of the disagreement between them at 300 K (reference isotherm). Furthermore,  
279 at low pressure ( $<25$  GPa) Speziale et al. 2001 diverges from other EOSs. This deviation is

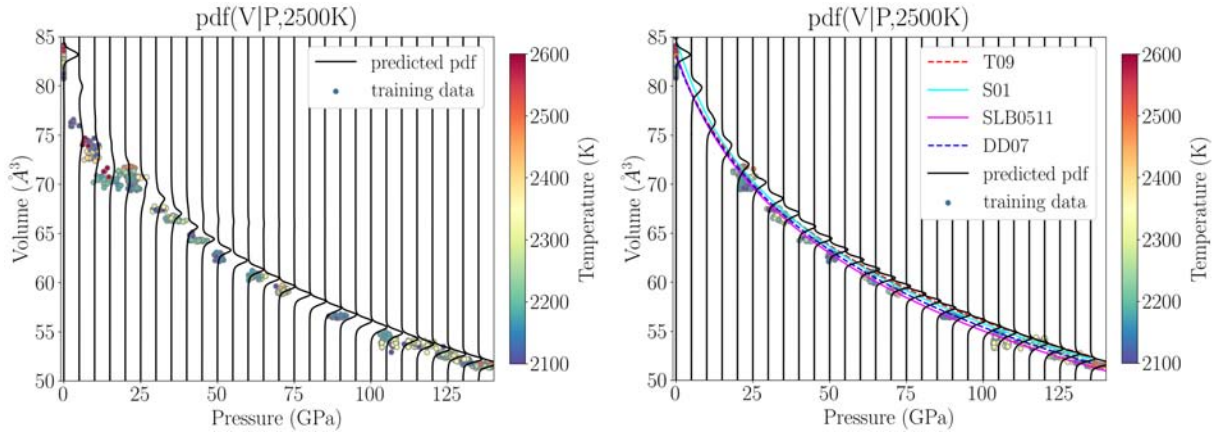


Figure 7: Left: pdfs for volume of MgO along a 2500 K isotherm predicted by MDNs trained with all data. Right: same as left but Fiquet et al. 1996 and Murakami et al. 2012 data are excluded. For comparison, volumes along the high temperature isotherm for some previously published EOSs (Tange et al. 2009, Speziale et al. 2001, Stixrude and Lithgow-Bertelloni 2005, 2011 and Dorogokupets and Dewaele 2007) are computed using MINUTI (Sturhahn 2020). On both panels we plot a sub-set of the total training data, namely those data at temperatures between 2100 and 2600 K. Excluding Fiquet et al. 1996 data from neural network training significantly reduces the width of the pdfs at high temperature and low pressure.

280 likely due to different values of fitting parameters together with distinct Grüneisen models to  
 281 compute the thermal behavior. For example, Speziale et al. 2001 do not consider anharmonic  
 282 effects, and their ambient Grüneisen parameters are also different than other studies (see  
 283 e.g. Ye et al. 2017, Dorogokupets and Dewaele 2007). Besides that, as with the case of the

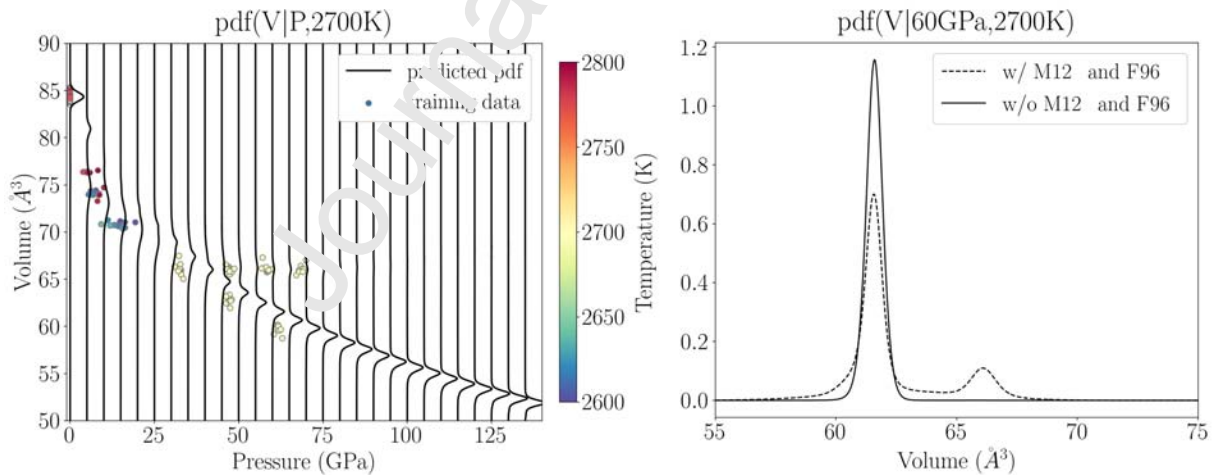


Figure 8: Left: pdfs for volume of MgO along a 2700 K isotherm predicted by the MDNs trained with all data. We also plot a sub-set of the training data, namely those whose temperatures lie between 2600 and 2800 K. Note: the large uncertainty in volume in the low pressure region (approximately below 25 GPa) is due to inclusion of data from Fiquet et al. 1996 as discussed in the text. Right: Comparison of posterior pdfs for volume predicted by MDNs trained with and without Murakami et al. 2012 (M12) and Fiquet et al. 1996 (F96) data at 2700 K and 60 GPa. The small peak at around  $66 \text{ \AA}^3$  is due to Murakami et al. 2012 data.

284 300 K isotherm, all explicit EOSs lie within the uncertainty range predicted by our MDNs,  
 285 which is expected because some training data come from the MgO pressure scales described  
 286 by these EOSs.

287 At 2700 K, the MDN predicted pdfs (Figure 8) show bimodal volumes in the pressure range  
 288 of approximately 45-90 GPa. Once we plot the associated training data on top, it becomes  
 289 clear that the smaller peaks in the pdfs are the representation of experimental data points  
 290 of Murakami et al. 2012. Surprisingly, for the same reported volume and temperature they  
 291 report pressures which are different from each other by about 36 GPa. However, their  
 292 reported densities appear to be physically reasonable. Nevertheless, we train another network  
 293 to discriminate how much uncertainty is coming from those specific data points. In doing  
 294 so, the posterior becomes unimodal. At 60 GPa, including Murakami et al. 2012 data leads  
 295 to a factor of approximately 3.5 wider pdfs for volume (Figure 8, right panel) compared to  
 296 results without those data. However, the effect of those data points seems to be local in  
 297 P-V-T space and their influence decreases for example, at higher pressures. This is because  
 298 MDNs interpolate locally in between samples, and data in one region of P-T space doesn't  
 299 influence uncertainties everywhere.

## 300 5. Bulk modulus and thermal expansivity

301 Since the training data do not contain explicit values for the volume derivatives with respect  
 302 to the inputs (P and T), getting constraints on bulk modulus ( $-V \frac{\partial P}{\partial V}$ ) and thermal expansivity  
 303 ( $\frac{1}{V} \frac{\partial V}{\partial T}$ ) is less straightforward than constraining the volumes. Hence, we follow a slightly  
 304 different approach compared to volume. We calculate the mean volume using Equation 6 for  
 305 any given P and T from each earlier obtained MDN. Then we perturb pressure ( $P + \delta P$ ) while  
 306 keeping the temperature fixed and compute the mean volume ( $\langle V(P + \delta P, T) \rangle$ ) for that  
 307 pressure from the same MDN. This way, we can compute the mean isothermal bulk modulus  
 308 ( $K$ ) as shown in Equation 7. Similarly, we evaluate mean volumes for two slightly different  
 309 temperatures but at a fixed pressure, and use that to compute the thermal expansivity,  $\alpha$

310 (Equation 8). For numerical differentiation, we use  $\delta P = 0.1$  GPa and  $\delta T = 1$  K. Using a  
 311 different value for  $\partial P$  or  $\partial T$  provides similar results.

$$312 \quad \langle K|P, T; \boldsymbol{\alpha} \rangle = \langle -V(P, T) \rangle \frac{\delta P}{\langle V(P + \delta P, T) \rangle - \langle V(P, T) \rangle} \quad (7)$$

$$313 \quad \langle \alpha|P, T; \boldsymbol{\alpha} \rangle = \frac{1}{\langle V(P, T) \rangle} \frac{\langle V(P, T + \delta T) \rangle - \langle V(P, T) \rangle}{\delta T} \quad (8)$$

315 Hence, in this approach, we take the derivatives of the P-V (or T-V) curve defined by the  
 316 mean of the posterior pdfs from each neural network rather than fitting P-V-T data to a  
 317 predefined EOS to get fitting parameters (such as  $K_{0T}$  and  $K'_{0T}$ ). Since we have trained a  
 318 large number of MDNs ( $10^3$ ) to predict the posterior pdf for volume, we get the same number  
 319 of mean isothermal bulk modulus and thermal expansivity values. This way, each neural  
 320 network approximates a slightly different mapping and its derivatives, and the distribution  
 321 on the mean bulk modulus and thermal expansivity can approximate the uncertainties on  
 322 them. Moreover, we use the same networks to compute the pdfs for volume and the mean  
 323 volumes; the volume that goes into the calculation of bulk modulus and thermal expansivity  
 324 is therefore consistent.

325 As an example, Figure 9 shows bulk modulus as a function of pressure along two selected  
 326 isotherms (refer to Appendix C.2 for other isotherms). The bulk modulus predicted by  
 327 neural networks shows a higher value at high pressure along the 300 K isotherm compared  
 328 to conventional EOSs. As mentioned earlier, this is likely due to the fact that the training  
 329 data come from experiments which make use of different EOSs and pressure standards than  
 330 those (MgO based) EOSs considered for comparison. Moreover, the fitting parameters ( $V_0$ ,  
 331  $K_{0T}$  and  $K'_{0T}$ ) are different for different EOSs. Hence, although these EOSs predict volume  
 332 within the uncertainty range predicted by MDNs (Figure 6, left panel), their derivatives  
 333 (Figure 6, right panel) differ significantly from each other and also from the MDN prediction,  
 334 leading to different values of bulk modulus.

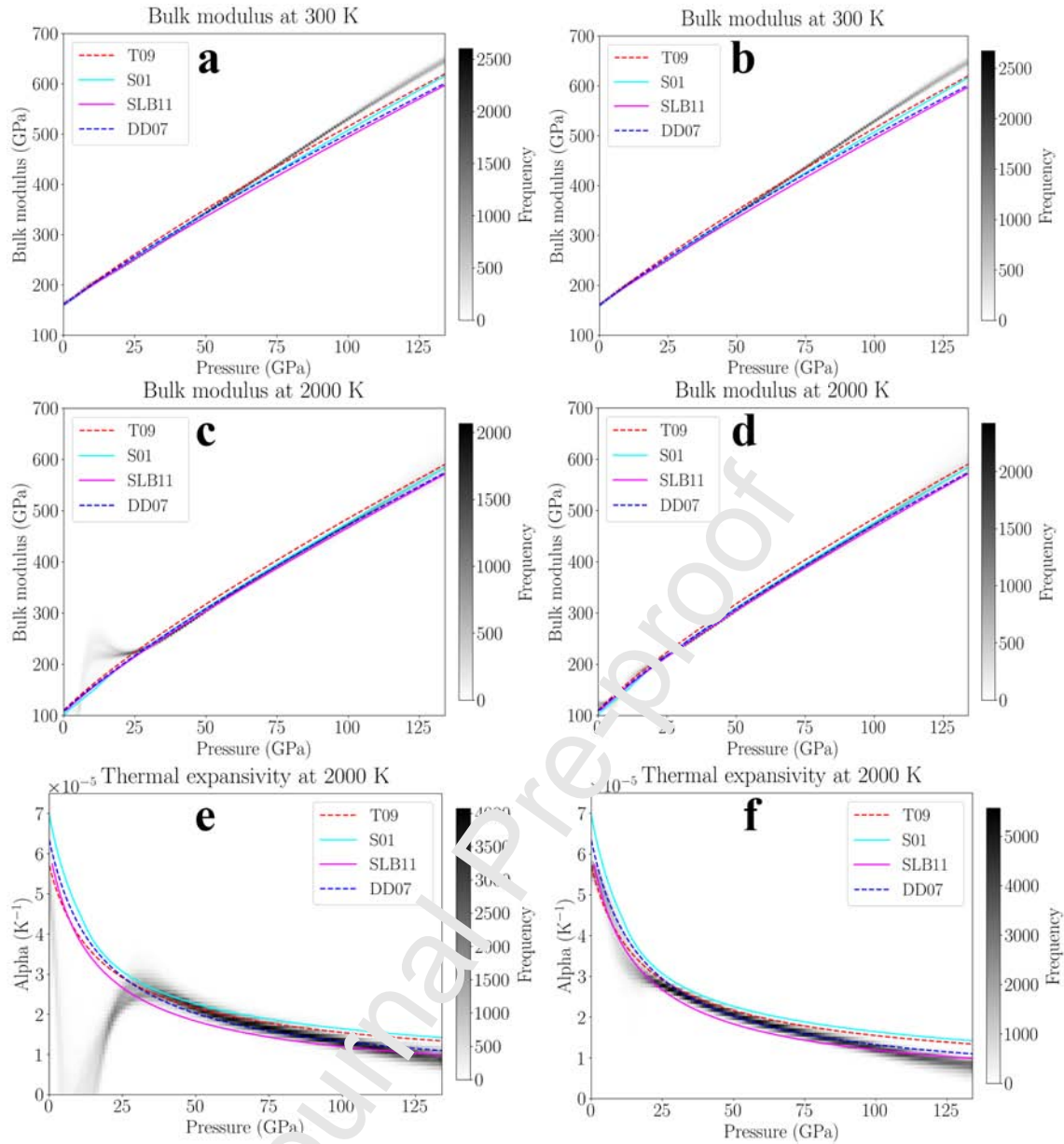


Figure 9: Comparison of the mean bulk modulus (a, b, c and d) and thermal expansivity (e and f) predicted by the neural networks with previously published equations of state for MgO (Tange et al. 2009, Speziale et al. 2001, Stixrude and Lithgow-Bertelloni 2011 and Dorogokupets and Dewaele 2007) as a function of pressure. The output from the neural networks is shown with greyscale- the darker the region of the plot, the greater the number of MDNs which predict the bulk modulus (or thermal expansivity) has that value. Frequency counts for output from the MDNs are at intervals of 1 GPa for pressure and bulk modulus, and  $10^{-7} \text{ K}^{-1}$  for thermal expansivity. For (a), (c) and (e) neural networks are trained with all collected data, whereas for (b), (d) and (f) data from Fiquet et al. 1996 and Murakami et al. 2012 have been excluded. Due to the inclusion of Fiquet et al. 1996 data we obtain large uncertainties in bulk modulus and thermal expansivity in low pressure, high temperature regions. Note: the overlapping of different EOSs makes the background histogram difficult to visualise.

335 One high temperature (2000 K) comparison between the neural network predicted mineral  
 336 properties and other studies is shown in Figure 9- c, d, e and f. In general, bulk modulus

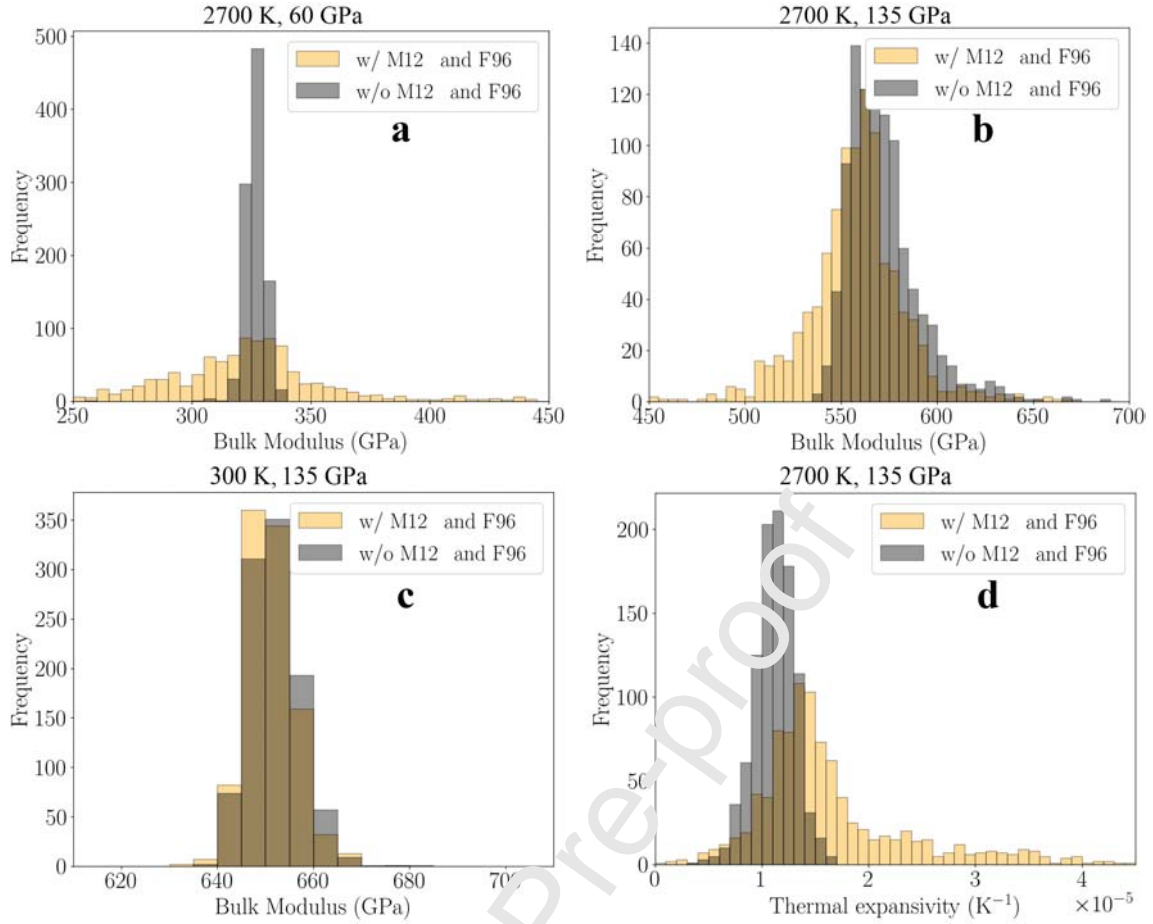


Figure 10: Comparison of the MDN predicted mean bulk modulus at (a) 2700 K, 60 GPa, (b) 2700 K, 135 GPa, (c) 300 K, 135 GPa and (d) thermal expansivity at 2700 K, 135 GPa of MgO trained with and without Murakami et al. 2012 (M12) and Fiquet et al. 1996 (F96). The effect of Murakami et al. 2012 data on bulk modulus and thermal expansivity is mainly around 2700 K, and it gradually reduces as pressure decreases or increases outside the interval approximately 45-90 GPa.

337 values predicted by the neural networks agree well with explicit EOSs, although Tange  
 338 et al. 2009 shows slightly higher values at moderate pressures (e.g. 60 GPa). The mean  
 339 bulk modulus predicted by the neural networks shows a large uncertainty at low pressures  
 340 (below  $\sim 25$  GPa) when high temperature data by Fiquet et al. 1996 are included. In  
 341 Figure 9- d, we show the bulk modulus predicted by the neural network trained without  
 342 Fiquet et al. 1996 (and Murakami et al. 2012). Here, the uncertainties at low pressure  
 343 are significantly decreased. Similarly, neural networks trained without those two data sets  
 344 predict physically reasonable thermal expansivities (Figure 9- f) compared to those trained  
 345 with all data sets (Figure 9- e). At high temperatures, we still see a sharp bend around 20  
 346 GPa (also see Appendix C) which we suggest may be related to anharmonic effects. As the

347 experimental data is relatively sparse in this region, one would need additional measurements  
348 (or theoretical studies) to confirm this. Furthermore, the thermal expansivity of Speziale  
349 et al. 2001 deviates from other EOSs. As mentioned in earlier studies (e.g. Dorogokupets  
350 and Dewaele 2007), this may be improved by including anharmonic terms in the EOS. In  
351 equation of state formalisms, one can add an anharmonic term to the total free energy. This  
352 additional term has a  $T^2$  dependence, rather than simply a linear temperature term. The  
353 effect of adding this term is most significant at low pressures, and can potentially capture  
354 more accurately the volume dependence at high temperatures compared with the standard  
355 thermal models without anharmonicity (for temperatures less than or equal to 2700 K in  
356 this meta dataset).

357 Besides low pressure, including Murakami et al. 2012 data during network training provides  
358 mean bulk modulus uncertainties that are more than 4 times larger (Figure 10- a) than  
359 excluding them together with Fiquet et al. 1996, and this discrepancy reduces at higher  
360 pressures (Figure 10- b). Moreover, as expected, neither Fiquet et al. 1996 nor Murakami  
361 et al. 2012 data influence bulk modulus at low temperatures, as shown in Figures 10- c and  
362 9- a, b.

## 363 6. Discussion

364 Fitting parameters (such as  $K_{0T}$  and  $K'_{0T}$ ) are inherent to explicit global EOSs, and a  
365 correlation between them tells us how one parameter changes with another providing optimal  
366 global fit. We do not estimate the uncertainties on fit parameters of EOSs which are specific  
367 to the underlying global functional form. Instead, we directly provide the uncertainties on  
368 volumes which are local in P-T space. The MDN is a kernel based method where we fit  
369 (a mixture of Gaussian) kernels to the experimental data and get an arbitrary probability  
370 density function on volume at any given P and T. The neural networks are flexible and  
371 interpolate locally; the uncertainties in one region of P-T space don't impact the posterior  
372 pdf everywhere. For example, Figure 7 shows no change in high pressure pdfs while removing

373 Fiquet et al. 1996 data in the region of low pressures. Our approach is also very powerful at  
374 identifying data inconsistencies when using different data sources.

375 The posterior pdfs given by the MDNs represent uncertainties in volume due to experi-  
376 mental errors, data gaps and data inconsistencies from different studies. Together with the  
377 uncertainties in mean isothermal bulk modulus and thermal expansivity, these results can  
378 be used by, for example, seismologists working on thermochemical interpretation of seismic  
379 data. Although uncertainties in volume, bulk modulus and thermal expansivity vary locally  
380 depending on sparsity and consistency of the experimental data, using these outputs from  
381 MDNs, one can directly compute bulk wave speed ( $\phi^2 = K_S/\rho$ ) and density ( $\rho$ ) at any given  
382 pressure and temperature. However, in order to compute bulk wave speeds at temperatures  
383 applicable to the lower mantle, we need the adiabatic bulk modulus ( $K_S = K_T(1 + \alpha\gamma T)$ ),  
384 where  $\gamma$  is Grüneisen parameter and  $\alpha$  is the thermal expansivity. Nevertheless, assuming  
385 that the difference between isothermal ( $K_T$ ) and adiabatic ( $K_S$ ) bulk moduli, at 300 K is  
386 roughly within  $\pm 1.0\%$  (Marquardt et al. 2018), the bulk wave speed of MgO is  $11.14 \pm 0.07$   
387 km/s at 135 GPa. At the same condition, the relative uncertainty (one standard deviation  
388 around mean) in density predicted by the MDNs is about  $\pm 1.0\%$ . This is larger than or  
389 comparable to the relative density variations in lower mantle estimated by previous studies  
390 (e.g. Ishii and Tromp 1999, Tromp et al. 2004, Koelemeijer et al. 2017). Although the  
391 Grüneisen parameter varies as a function of volume that ultimately depends on pressure  
392 (and temperature), we assume it to be approximately  $1.1 \pm 0.3$  (e.g. Stixrude and Lithgow-  
393 Bertelloni 2011, Ye et al. 2017) at 2700 K and 135 GPa to give an estimate of uncertainties  
394 in bulk wave speed. In doing so, the relative uncertainty in bulk wave speed is about  $\pm 1.77\%$   
395 which is larger than the reported bulk sound speed variation in the lower mantle (e.g. Tromp  
396 pert et al. 2004).

397 Estimation of mineral properties beyond the range of experimental data requires extrapola-  
398 tion. The standard EOSs can easily be used for extrapolation provided that the assumptions  
399 of the functional form hold in the region of no data. In general, it has been observed that

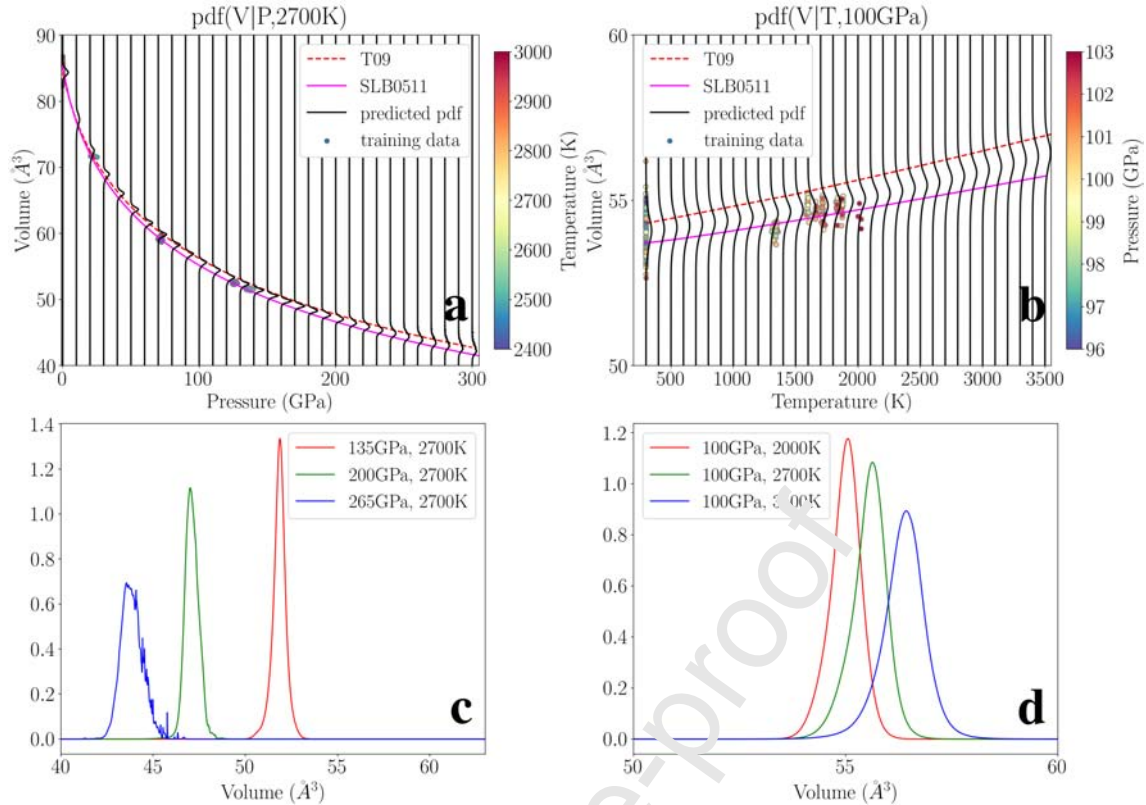


Figure 11: Probability density function for volume of MgO along a 2700 K isotherm (a) and 100 GPa isobar (b). Training data belonging to temperature between 2400 and 3000 K (a), and pressure range from 96 to 103 GPa (b) are also shown. Magenta (SLB0511) and red (T09) curves are Stixrude and Lithgow-Bertelloni 2005, 2011 and Tange et al. 2009 EOS, respectively. They follow the volume trend predicted by the network. In the region outside the prior data, the trained MDNs provide wider pdfs as they are forced to extrapolate the volume. To illustrate this more clearly, volume pdfs at a fixed temperature (and pressure) and three different pressure (and temperature) are also shown in c (and d).

400 MDNs provide a wider estimate of uncertainties in the region of little to no training data  
 401 (Käuffl et al. 2016a). Here also as shown by the wider pdfs in Figure 11, the uncertainty  
 402 in predicted mineral properties increases when the network has to extrapolate from distant  
 403 training data. We note that EOSs of Stixrude and Lithgow-Bertelloni 2005, 2011 and Tange  
 404 et al. 2009 closely follow the pdf predicted by the network indicating that it learns a func-  
 405 tional form present in the data, but errs on the cautious side by returning larger uncertainties.  
 406 From a Bayesian perspective, we would advise against extrapolation as this covers a region  
 407 outside the prior. Figure 11, however, demonstrates some capability of neural networks to  
 408 extrapolate beyond the ranges of the data, although we would need to establish how far this  
 409 is related to the precise network architecture.

410 The shear modulus is required to calculate compressional and shear wave speeds. There is no  
411 thermodynamic expression for the shear modulus, but functional forms are often assumed,  
412 for example third order finite-strain and shear counterpart of the Keane EOSs (Keane 1954)  
413 by Kennett 2017, to compute the shear modulus which are based on the bulk modulus  
414 calculation. One can also use the linear relationship among shear modulus, adiabatic bulk  
415 modulus and pressure given by Stacey 1995. However, the uncertainties in shear modulus  
416 would then be dependent on those in bulk modulus, and the assumption that shear properties  
417 can be constrained from the bulk properties. An alternative is to use data from experiments  
418 such as Brillouin Spectroscopy that provide shear wave speed information. Together with  
419 unit-cell volume, as measured by X-ray diffraction on the same sample (e.g. Murakami et al.  
420 2012, Kurnosov et al. 2017) and known sample composition, the density and thus shear  
421 moduli can be determined. However, these data sets do not cover simultaneous high pressure  
422 and temperature regions that are expected in the Earth's lowermost mantle. For example,  
423 the highest temperature and pressure data for MgO reported in Murakami et al. 2012 are  
424 six measurements at 2700 K and between 32.5-68.4 GPa. Nevertheless, a combination of  
425 wave speed data from ultrasonic techniques and Brillouin Spectroscopy together with high  
426 P-V-T data from x-ray diffraction techniques has the potential to exhaustively sample the  
427 lower mantle geotherm in the near future (Marquardt and Thomson 2020).

428 We note that, in principle, a combination of experimental data and theoretical calculations  
429 (e.g. Karki et al. 1999, Oganov and Dorogokupets 2003, Wu et al. 2008) is possible. This may  
430 provide additional constraints on the predicted mineral properties covering a wider range of  
431 pressure and temperature. Since our approach implicitly identifies the consistency between  
432 different data sources, a proper rationale can be developed to mix data and uncertainties from  
433 theory with experiments. Furthermore, the MDN based approach can easily be extended to  
434 the upper mantle and the core. Since MDNs are flexible, they can be employed to model  
435 multi-mode targets/outputs. This would be helpful to model for example volume anomalies  
436 induced by the iron spin transition (e.g. Marquardt et al. 2009, Speziale et al. 2007, Lin  
437 et al. 2006, Crowhurst et al. 2008, Solomatova et al. 2016). A natural progression of this

438 work is to extend it for solid solution. It is straightforward to include composition, e.g. the  
439 Mg/Fe ratio, by including it as an extra dimension in the input data (i.e. P, T and mol% Fe  
440 in ferropericlasite) provided there is enough training data.

## 441 7. Conclusions

442 This study demonstrates the feasibility of a neural network based approach to infer the  
443 material properties of lower mantle minerals. In our approach, we learn the underlying P-V-  
444 T relationship providing a reasonable approximation of the P-v-T data of MgO. This allows  
445 us to compute the uncertainties in density, thermal expansivity and bulk modulus without  
446 prescribing an explicit EOS. Once the networks are trained, it is a simple function that can  
447 be evaluated at any given pressure and temperature to get volume, mean bulk modulus and  
448 thermal expansivity with uncertainties. In order to train the networks, we collect data from  
449 high P-V-T experiments without prior selection of data (e.g. based on pressure scale or  
450 functional form used). Hence, our uncertainties are not biased towards a subjective selection  
451 of experimental data. Furthermore, our approach identifies inconsistencies between data  
452 from different sources. The assumption that an EOS follows a particular form provides a  
453 priori information by fixing their form (or thermodynamic model) and/or pressure scale.  
454 It remains to be determined which EOS form best describes the thermodynamic behaviour  
455 of MgO at wide range of pressures and temperatures. In this study, we compare a few  
456 "standard" EOSs with the material properties inferred from neural networks and show that  
457 choosing one particular explicit form provides a biased estimate of uncertainties.

458 Based on the prediction performance of the MDNs and comparison with conventional EOSs  
459 (such as Figures 3, 7, 9, and Appendix C), we can be most confident about physical inter-  
460 pretation of seismic data in the lower mantle within the prior range of experimental data  
461 (Figure 2). In the regions where there exists little evidence about how the P-V-T relationship  
462 behaves, such as at low pressure, high temperature ( $<25$  GPa,  $>1500$  K), and temperatures  
463 approximately  $>2700$  K at pressures expected towards the core-mantle boundary, neural

464 networks show increasingly uncertain predictions. Although for the Earth's lower mantle,  
 465 low pressure and high temperature environments may not be relevant, they are expected in  
 466 other planetary bodies such as the Moon and Mars (e.g. Khan et al. 2014, 2018). With  
 467 currently available data, it likely provides meaningful uncertainties that could be used by  
 468 seismologists within certain ranges of pressure and temperature, while highlighting the P,  
 469 T regions in which more experimental (or theoretical) data is needed before we can draw  
 470 robust conclusions on temperature and composition.

## 471 Acknowledgements

472 We would like to thank an anonymous reviewer for helpful comments which improved the  
 473 manuscript. AR and LC received funding from the Dutch Research Council (NWO) on grant  
 474 number 016.Vidi.171.022. JMJ is thankful for discussions with Wolfgang Sturhahn and for  
 475 support of this research by the National Science Foundation's Collaborative Studies of the  
 476 Earth's Deep Interior (EAR-1161046 and FAR-2009735).

## 477 Appendices

### 478 Appendix A. Generalised theory of the MDN

479 Let,  $\mathbf{x} = \{x_1, x_2, \dots, x_I\}$  be the input data to the feed-forward part of the MDN. Please note,  
 480 to generalise this section, we write inputs as  $\mathbf{x}$  and targets as  $m_k$  instead of P & T and V,  
 481 respectively. The feed-forward network outputs  $y_k$  are computed as a weighted sum of the  
 482 outputs from the hidden nodes plus a bias

$$483 \quad y_k = f_2 \left( \sum_{j=1}^J \alpha_{jk} h_j + \alpha_{0k} \right) \quad (\text{A.1})$$

484 where the function  $f_2$  is an identity function such that  $f_2(p) = p$ ,  $\alpha_{jk}$  is the hidden layer  
 485 weight matrix and  $\alpha_{0k}$  represents a bias term of each output node. Now, the hidden node

486 outputs  $h_j$  are computed as

$$487 \quad h_j = f_1 \left( \sum_{i=1}^I \alpha_{ij} x_i + \alpha_{0j} \right) \quad (\text{A.2})$$

488 where the function  $f_1$  is a logistic sigmoid function  $f_1(p) = \frac{1}{1+\exp(-p)}$ ,  $\alpha_{ij}$  is the input layer  
 489 weight matrix,  $\alpha_{0j}$  are the biases of hidden nodes and  $x_i$  are input data.  $y_k$  are related to  
 490 the parameters, namely weights ( $\pi_n$ ), means ( $\mu_n$ ) and standard deviations ( $\sigma_n$ ) of Gaussians  
 491 in the Gaussian Mixture Model (GMM) by the following relationship (for details see e.g.  
 492 Bishop 1994, de Wit et al. 2013)

$$493 \quad \pi_n(\mathbf{x}; \boldsymbol{\alpha}) = \frac{\exp(y_k^{(\pi)}(\mathbf{x}; \boldsymbol{\alpha}))}{\sum_{n=1}^M \exp(y_n^{(\pi)}(\mathbf{x}; \boldsymbol{\alpha}))}, \quad (\text{A.3})$$

$$494 \quad \mu_n(\mathbf{x}; \boldsymbol{\alpha}) = y_k^{(\mu)}(\mathbf{x}; \boldsymbol{\alpha}) \text{ and} \quad (\text{A.4})$$

$$495 \quad \sigma_n(\mathbf{x}; \boldsymbol{\alpha}) = \exp(y_k^{(\sigma)}(\mathbf{x}; \boldsymbol{\alpha})). \quad (\text{A.5})$$

## 498 Appendix B. MDN initialization and training details

499 The total data ( $\mathbf{x}$ ) is divided into three sets- training (70%), monitoring (20%) and test  
 500 (10%) sets such that

$$501 \quad \mathbf{x}^{train} \subset \mathbf{x}, \mathbf{x}^{monitor} \subset \mathbf{x} \text{ and } \mathbf{x}^{test} \subset \mathbf{x} \quad (\text{B.1})$$

502 with  $\mathbf{x}^{train} \cap \mathbf{x}^{monitor} = \emptyset$ ,  $\mathbf{x}^{train} \cap \mathbf{x}^{test} = \emptyset$  and  $\mathbf{x}^{monitor} \cap \mathbf{x}^{test} = \emptyset$ . Using the training  
 503 data ( $\mathbf{x}^{train}$ ) we train the MDN. However, before we train the MDN we need to decide on  
 504 initial values of the network parameters. We randomly draw the input layer and hidden layer  
 505 weights (Bishop 1995) according to the following Gaussian distributions

$$506 \quad \alpha_{ij} \sim \mathcal{N}\left(0, \frac{1}{I+1}\right) \quad (\text{B.2})$$

507 and

$$508 \quad \alpha_{jk} \sim \mathcal{N}\left(0, \frac{1}{J+1}\right), \quad (\text{B.3})$$

509 respectively. Where I and J are number of input and hidden nodes, respectively. Similarly,  
 510 the output layer biases are initialized by a K-means clustering algorithm (i.e. fitting a  
 511 GMM to the training data set). Once the initialization is done and the training begins,  
 512 the difference between the output and the target can be computed according to the error  
 513 function

$$514 \quad E^{train} = \sum_{train} -\ln\left(p(m_k|\mathbf{x}^{train}; \boldsymbol{\alpha})\right) \quad (\text{B.4})$$

515 which is summed over all training data providing the average error. This function is also  
 516 called the loss function which is minimized iteratively using the ADAM optimization method  
 517 (see detailed algorithm in Kingma and Ba 2014). The explicit dependence of output posterior  
 518 on the network parameters (see Käuffl et al. 2016a and references therein) can be avoided by  
 519 using multiple MDNs and combining them by weighted sum. The weight of each MDN is  
 520 determined by the test set error as

$$521 \quad w_i = \exp\left(-\frac{E^{test}(\mathbf{x}^{test}, \boldsymbol{\alpha}_i)}{N}\right) \quad (\text{B.5})$$

522 where index  $i$  denotes the  $i$ -th MDN ( $C$  MDNs in total) and  $N$  is the size of the test data  
 523 set, and the MDNs are combined according to

$$524 \quad p(m_k|\mathbf{x}; \boldsymbol{\alpha}) = \frac{\sum_{i=1}^C w_i}{\sum_j w_j} p_i(m_k|\mathbf{x}; \boldsymbol{\alpha}_i). \quad (\text{B.6})$$

## 525 **Appendix C. Mineral properties**

### 526 *Appendix C.1. P-V-T EOS*

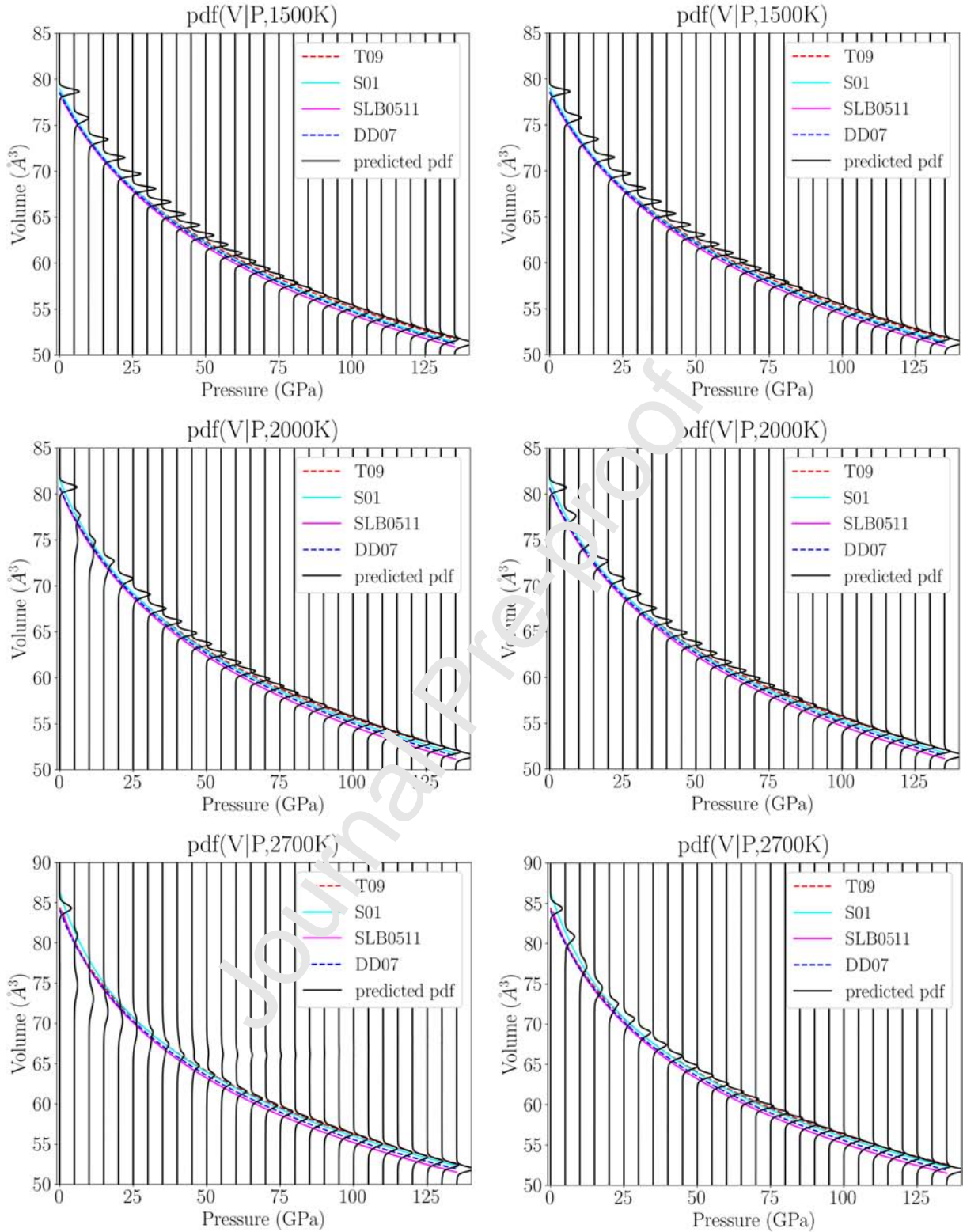


Figure Appendix C.1: P-V relationship of MgO predicted by MDNs trained with (left) all data and (right) excluding Murakami et al. 2012 and Fiquet et al. 1996. Comparison with previously published EOSs (Tange et al. 2009, Speziale et al. 2001, Stixrude and Lithgow-Bertelloni 2005, 2011 and Dorogokupets and Dewaele 2007) along 1500 K (top), 2000 K (middle) and 2700 K (bottom) isotherms also shown.

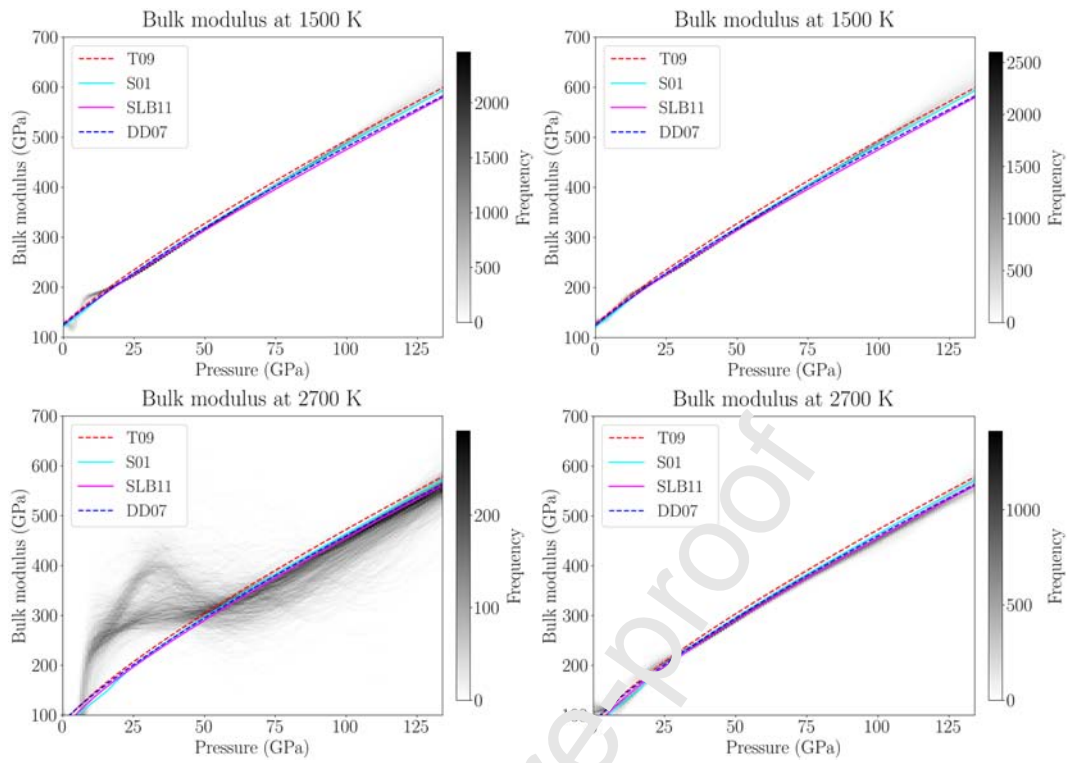
527 *Appendix C.2. Bulk modulus*

Figure Appendix C.2: Comparison of the bulk modulus of MgO predicted by the neural network along 1500 K (top) and 2700 K (bottom) isotherms with other studies (Tange et al. 2009, Speziale et al. 2001, Stixrude and Lithgow-Bertelloni 2011 and Dorogokupets and Dewaele 2007) as a function of pressure. Left panel shows results from MDNs trained with all data and the right panel shows results from MDNs excluding Murakami et al. 2012 and Fiquet et al. 19% data in training.

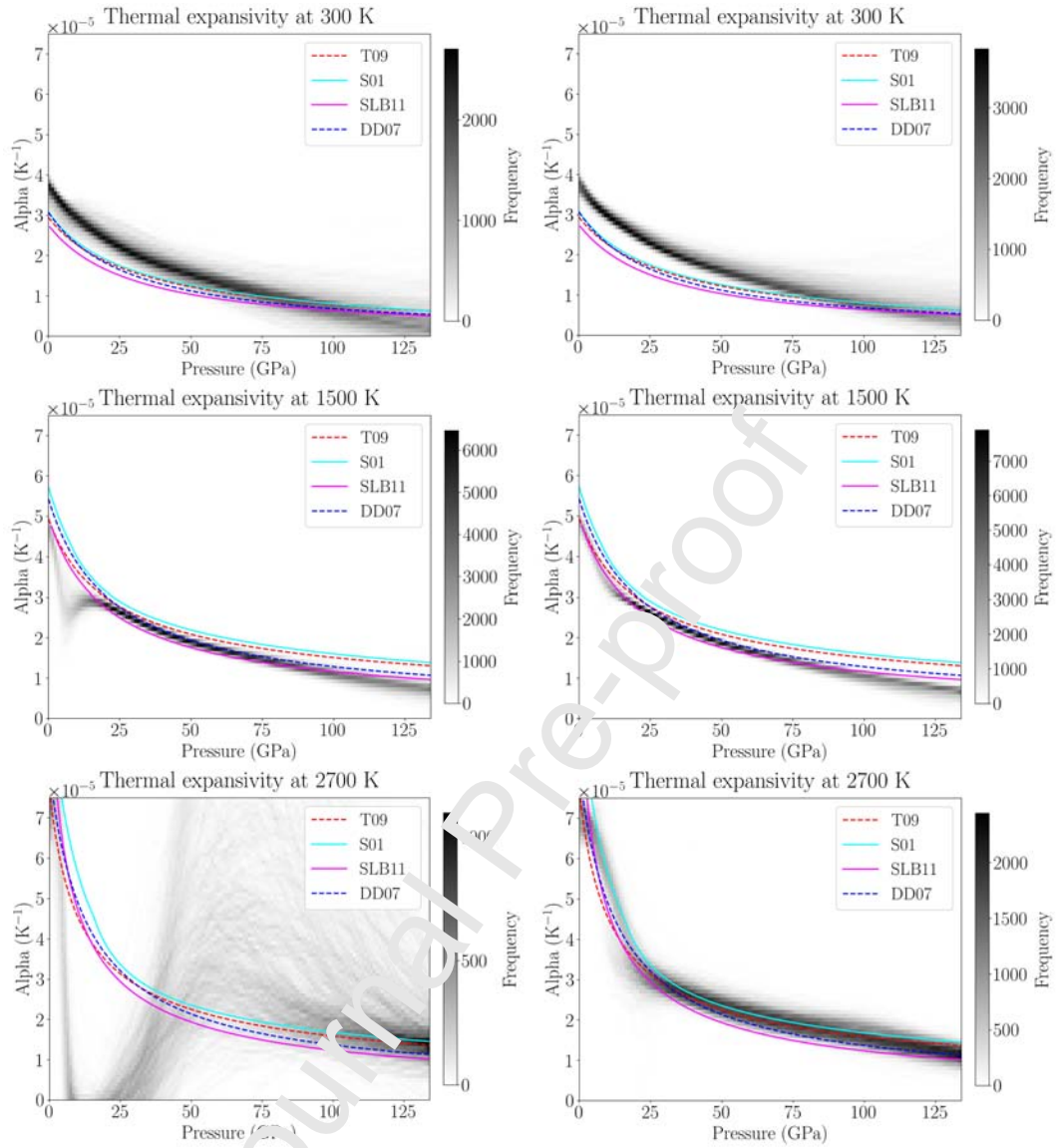


Figure Appendix C.3: Comparison of the thermal expansivity of MgO predicted by neural networks with Tange et al. 2009, Stixrude and Lithgow-Bertelloni 2011 and Dorogokupets and Dewaele 2007 along 300 K (top), 1500 K (middle) and 2700 K (bottom) isotherms as a function of pressure. Left panel: MDNs trained with all data. Right: MDNs trained without Murakami et al. 2012 and Fiquet et al. 1996 data.

529 **References**

- 530 M. Abadi, A. Agarwal, P. Barham, E. Brevdo, Z. Chen, C. Citro, G. S. Corrado, A. Davis,  
531 J. Dean, M. Devin, S. Ghemawat, I. Goodfellow, A. Harp, G. Irving, M. Isard, Y. Jia,  
532 R. Jozefowicz, L. Kaiser, M. Kudlur, J. Levenberg, D. Mané, R. Monga, S. Moore, D. Mur-  
533 ray, C. Olah, M. Schuster, J. Shlens, B. Steiner, I. Sutskever, K. Talwar, P. Tucker, V. Van-  
534 houcke, V. Vasudevan, F. Viégas, O. Vinyals, P. Warden, M. Wattenberg, M. Wicke, Y. Yu,  
535 and X. Zheng. TensorFlow: Large-scale machine learning on heterogeneous systems, 2015.  
536 URL <https://www.tensorflow.org/>. Software available from tensorflow.org.
- 537 S. Atkins, A. P. Valentine, P. J. Tackley, and J. Trampert. Using pattern recognition to infer  
538 parameters governing mantle convection. *Physics of the Earth and Planetary Interiors*,  
539 257:171 – 186, 2016. ISSN 0031-9201. doi: <https://doi.org/10.1016/j.pepi.2016.05.016>.  
540 URL <http://www.sciencedirect.com/science/article/pii/S0031920116300863>.
- 541 C. Bishop. *Neural Networks for Pattern Recognition*. Oxford University Press,  
542 January 1995. URL [https://www.microsoft.com/en-us/research/publication/  
543 neural-networks-pattern-recognition-2/](https://www.microsoft.com/en-us/research/publication/neural-networks-pattern-recognition-2/).
- 544 C. M. Bishop. Mixture density networks. Technical report, Aston University, Birmingham,  
545 1994.
- 546 F. Cammarano, S. Goes, P. Vacher, and D. Giardini. Inferring upper-mantle temperatures  
547 from seismic velocities. *Physics of the Earth and Planetary Interiors*, 138(3):197 – 222,  
548 2003. ISSN 0031-9201. doi: [https://doi.org/10.1016/S0031-9201\(03\)00156-0](https://doi.org/10.1016/S0031-9201(03)00156-0). URL [http:  
549 //www.sciencedirect.com/science/article/pii/S0031920103001560](http://www.sciencedirect.com/science/article/pii/S0031920103001560).
- 550 F. Cammarano, A. Deuss, S. Goes, and D. Giardini. One-dimensional physical reference  
551 models for the upper mantle and transition zone: Combining seismic and mineral physics  
552 constraints. *Journal of Geophysical Research: Solid Earth*, 110(B1), 2005a. doi: 10.1029/  
553 2004JB003272. URL [https://agupubs.onlinelibrary.wiley.com/doi/abs/10.1029/  
554 2004JB003272](https://agupubs.onlinelibrary.wiley.com/doi/abs/10.1029/2004JB003272).

- 555 F. Cammarano, S. Goes, A. Deuss, and D. Giardini. Is a pyrolytic adiabatic mantle  
556 compatible with seismic data? *Earth and Planetary Science Letters*, 232(3):227 –  
557 243, 2005b. ISSN 0012-821X. doi: <https://doi.org/10.1016/j.epsl.2005.01.031>. URL  
558 <http://www.sciencedirect.com/science/article/pii/S0012821X05000804>.
- 559 L. Cobden, S. Goes, F. Cammarano, and J. A. D. Connolly. Thermochemical interpreta-  
560 tion of one-dimensional seismic reference models for the upper mantle: Evidence for bias  
561 due to heterogeneity. *Geophysical Journal International*, 175(2):627–648, 11 2008. ISSN  
562 0956-540X. doi: 10.1111/j.1365-246X.2008.03903.x. URL [https://doi.org/10.1111/j.](https://doi.org/10.1111/j.1365-246X.2008.03903.x)  
563 [1365-246X.2008.03903.x](https://doi.org/10.1111/j.1365-246X.2008.03903.x).
- 564 L. Cobden, S. Goes, M. Ravenna, E. Styles, F. Cammarano, K. Gallagher, and J. A. D.  
565 Connolly. Thermochemical interpretation of 1-D seismic data for the lower mantle: The  
566 significance of nonadiabatic thermal gradients and compositional heterogeneity. *Journal*  
567 *of Geophysical Research: Solid Earth*, 114(B12), 2009. doi: 10.1029/2008JB006262. URL  
568 <https://agupubs.onlinelibrary.wiley.com/doi/abs/10.1029/2008JB006262>.
- 569 J. C. Crowhurst, J. M. Brown, A. F. Goncharov, and S. D. Jacobsen. Elasticity of (mg,fe)o  
570 through the spin transition of iron in the lower mantle. *Science*, 319(5862):451–453, 2008.  
571 ISSN 0036-8075. doi: 10.1126/science.1149606. URL [https://science.sciencemag.](https://science.sciencemag.org/content/319/5862/451)  
572 [org/content/319/5862/451](https://science.sciencemag.org/content/319/5862/451).
- 573 G. Cybenko. Approximation by superpositions of a sigmoidal function. *Mathematics of*  
574 *Control, Signals and Systems*, 2(4):303–314, Dec 1989. doi: 10.1007/BF02551274. URL  
575 <https://doi.org/10.1007/BF02551274>.
- 576 R. de Wit and J. Trampert. Robust constraints on average radial lower mantle anisotropy  
577 and consequences for composition and texture. *Earth and Planetary Science Letters*, 429:  
578 101 – 109, 2015. ISSN 0012-821X. doi: <https://doi.org/10.1016/j.epsl.2015.07.057>. URL  
579 <http://www.sciencedirect.com/science/article/pii/S0012821X15005002>.
- 580 R. de Wit, P. Käuffl, A. Valentine, and J. Trampert. Bayesian inversion of free oscillations

- 581 for earth's radial (an)elastic structure. *Physics of the Earth and Planetary Interiors*, 237:  
582 1 – 17, 2014. ISSN 0031-9201. doi: <https://doi.org/10.1016/j.pepi.2014.09.004>. URL  
583 <http://www.sciencedirect.com/science/article/pii/S0031920114002039>.
- 584 R. W. L. de Wit, A. P. Valentine, and J. Trampert. Bayesian inference of Earth's radial  
585 seismic structure from body-wave traveltimes using neural networks. *Geophysical Journal  
586 International*, 195(1):408–422, 06 2013. ISSN 0956-540X. doi: 10.1093/gji/ggt220. URL  
587 <https://doi.org/10.1093/gji/ggt220>.
- 588 F. Deschamps and J. Trampert. Towards a lower mantle reference temperature and com-  
589 position. *Earth and Planetary Science Letters*, 222(1):161 – 175, 2004. ISSN 0012-821X.  
590 doi: <https://doi.org/10.1016/j.epsl.2004.02.024>. URL [http://www.sciencedirect.com/  
591 science/article/pii/S0012821X04001426](http://www.sciencedirect.com/science/article/pii/S0012821X04001426).
- 592 F. Deschamps, L. Cobden, and P. J. Tackley. The primitive nature of large low shear-  
593 wave velocity provinces. *Earth and Planetary Science Letters*, 349-350:198 – 208, 2012.  
594 ISSN 0012-821X. doi: <https://doi.org/10.1016/j.epsl.2012.07.012>. URL [http://www.  
595 sciencedirect.com/science/article/pii/S0012821X12003718](http://www.sciencedirect.com/science/article/pii/S0012821X12003718).
- 596 A. Dewaele, G. Fiquet, D. Andrault, and D. Hausermann. P-V-T equation of state of  
597 periclase from synchrotron radiation measurements. *Journal of Geophysical Research:  
598 Solid Earth*, 105(B2):2869–2877, 2000. doi: 10.1029/1999JB900364.
- 599 V. V. Dobrosavljevic, W. Sturhahn, and J. M. Jackson. Evaluating the role of iron-rich  
600 (Mg,Fe)O in ultralow velocity zones. *Minerals*, 9(12), 2019. doi: 10.3390/min9120762.  
601 URL <https://www.mdpi.com/2075-163X/9/12/762>.
- 602 S. M. Dorfman, V. B. Prakapenka, Y. Meng, and T. S. Duffy. Intercomparison of pressure  
603 standards (Au, Pt, Mo, MgO, NaCl and Ne) to 2.5 Mbar. *Journal of Geophysical Research:  
604 Solid Earth*, 117(B8), 2012. doi: 10.1029/2012JB009292.
- 605 P. I. Dorogokupets and A. Dewaele. Equations of state of MgO, Au, Pt, NaCl-B1, and NaCl-  
606 B2: Internally consistent high-temperature pressure scales. *High Pressure Research*, 27

- 607 (4):431–446, 2007. doi: 10.1080/08957950701659700. URL <https://doi.org/10.1080/>  
608 08957950701659700.
- 609 L. Dubrovinsky and S. Saxena. Thermal expansion of periclase (MgO) and tungsten (W) to  
610 melting temperatures. *Physics and Chemistry of Minerals*, 24(8):547–550, 1997.
- 611 T. Duffy and Y. Wang. Pressure-volume-temperature equation of state. *Reviews in Miner-*  
612 *alogy*, 37, 1998.
- 613 T. S. Duffy and T. J. Ahrens. Compressional sound velocity equation of state, and consti-  
614 tutive response of shock-compressed magnesium oxide. *Journal of Geophysical Research:*  
615 *Solid Earth*, 100(B1):529–542, 1995. doi: 10.1029/94JB02965.
- 616 A. M. Dziewonski and D. L. Anderson. Preliminary reference earth model. *Physics*  
617 *of the Earth and Planetary Interiors*, 25(4):297–356, 1981. ISSN 0031-9201. doi:  
618 [https://doi.org/10.1016/0031-9201\(81\)90046-7](https://doi.org/10.1016/0031-9201(81)90046-7). URL [http://www.sciencedirect.com/](http://www.sciencedirect.com/science/article/pii/0031920181900467)  
619 [science/article/pii/0031920181900467](http://www.sciencedirect.com/science/article/pii/0031920181900467).
- 620 S. Earp and A. Curtis. Probabilistic neural network-based 2D travel-time tomography. *Neural*  
621 *Computing and Applications*, 32:17077–17095, 2020. doi: 10.1007/s00521-020-04921-8.  
622 URL <https://doi.org/10.1007/s00521-020-04921-8>.
- 623 D. Fan, S. Fu, J. Yang, S. Tkachev, V. Prakapenka, and J.-F. Lin. Elasticity of single-crystal  
624 periclase at high pressure and temperature: The effect of iron on the elasticity and seismic  
625 parameters of ferropericlase in the lower mantle. *American Mineralogist*, 104:262–275, 02  
626 2019. doi: 10.2138/am-2019-6656.
- 627 Y. Fei. Effects of temperature and composition on the bulk modulus of (Mg,Fe)O. *American*  
628 *Mineralogist*, 84:272–276, 1999.
- 629 Y. Fei, J. Li, K. Hirose, W. Minarik, J. V. Orman, C. Sanloup, W. van Westrenen,  
630 T. Komabayashi, and K. ichi Funakoshi. A critical evaluation of pressure scales at high

- 631 temperatures by in situ x-ray diffraction measurements. *Physics of the Earth and Plan-*  
632 *etary Interiors*, 143-144:515 – 526, 2004a. ISSN 0031-9201. doi: [https://doi.org/10.](https://doi.org/10.1016/j.pepi.2003.09.018)  
633 [1016/j.pepi.2003.09.018](https://doi.org/10.1016/j.pepi.2003.09.018). URL [http://www.sciencedirect.com/science/article/pii/](http://www.sciencedirect.com/science/article/pii/S0031920104000858)  
634 [S0031920104000858](http://www.sciencedirect.com/science/article/pii/S0031920104000858). New Developments in High-Pressure Mineral Physics and Applica-  
635 tions to the Earth's Interior.
- 636 Y. Fei, J. Van Orman, J. Li, W. van Westrenen, C. Sanloup, W. Minarik, K. Hirose,  
637 T. Komabayashi, M. Walter, and K. Funakoshi. Experimentally determined postspinel  
638 transformation boundary in  $Mg_2SiO_4$  using  $MgO$  as an internal pressure standard and its  
639 geophysical implications. *Journal of Geophysical Research: Solid Earth*, 109(B2), 2004b.  
640 doi: [10.1029/2003JB002562](https://doi.org/10.1029/2003JB002562). URL [https://agupubs.onlinelibrary.wiley.com/doi/](https://agupubs.onlinelibrary.wiley.com/doi/abs/10.1029/2003JB002562)  
641 [abs/10.1029/2003JB002562](https://agupubs.onlinelibrary.wiley.com/doi/abs/10.1029/2003JB002562).
- 642 G. Fiquet, D. Andrault, J. Itié, P. Gillet, and P. Richet. X-ray diffraction of periclase in  
643 a laser-heated diamond-anvil cell. *Physics of the Earth and Planetary Interiors*, 95(1):1  
644 – 17, 1996. ISSN 0031-9201. doi: [https://doi.org/10.1016/0031-9201\(95\)03109-X](https://doi.org/10.1016/0031-9201(95)03109-X). URL  
645 <http://www.sciencedirect.com/science/article/pii/003192019503109X>.
- 646 G. Fiquet, P. Richet, and G. Montagnac. High-temperature thermal expansion of lime,  
647 periclase, corundum and spinel. *Physics and Chemistry of Minerals*, 27:103–111, 12 1999.  
648 doi: [10.1007/s002690050246](https://doi.org/10.1007/s002690050246). URL <https://doi.org/10.1007/s002690050246>.
- 649 R. A. Forman, G. J. Piermarini, J. D. Barnett, and S. Block. Pressure measurement made  
650 by the utilization of ruby sharp-line luminescence. *Science*, 176(4032):284–285, 1972. doi:  
651 [10.1126/science.176.4032.284](https://doi.org/10.1126/science.176.4032.284). URL [https://science.sciencemag.org/content/176/](https://science.sciencemag.org/content/176/4032/284)  
652 [4032/284](https://science.sciencemag.org/content/176/4032/284).
- 653 E. J. Garnero and D. V. Helmberger. Further structural constraints and uncertainties of  
654 a thin laterally varying ultralow-velocity layer at the base of the mantle. *Journal of*  
655 *Geophysical Research: Solid Earth*, 103(B6):12495–12509, 1998. doi: <https://doi.org/>

656 10.1029/98JB00700. URL <https://agupubs.onlinelibrary.wiley.com/doi/abs/10.1029/98JB00700>.

658 E. J. Garnero, A. K. McNamara, and S.-H. Shim. Continent-sized anomalous zones with low  
659 seismic velocity at the base of earth's mantle. *Nature Geoscience*, 9:481–489, 2016. doi:  
660 10.1038/ngeo2733. URL <https://doi.org/10.1038/ngeo2733>.

661 J. W. Hernlund and C. Houser. On the statistical distribution of seismic velocities in  
662 earth's deep mantle. *Earth and Planetary Science Letters*, 265(3):423 – 437, 2008.  
663 ISSN 0012-821X. doi: <https://doi.org/10.1016/j.epsl.2008.10.042>. URL <http://www.sciencedirect.com/science/article/pii/S0012821X08005784>.

665 K. Hirose, N. Sata, T. Komabayashi, and Y. Ohishi. Simultaneous volume measure-  
666 ments of Au and MgO to 140GPa and thermal equation of state of Au based on  
667 the MgO pressure scale. *Physics of the Earth and Planetary Interiors*, 167(3):149 –  
668 154, 2008. ISSN 0031-9201. doi: <https://doi.org/10.1016/j.pepi.2008.03.002>. URL  
669 <http://www.sciencedirect.com/science/article/pii/S0031920108000460>.

670 K. Hornik, M. Stinchcombe, and H. White. Multilayer feedforward networks are uni-  
671 versal approximators. *Neural Networks*, 2(5):359 – 366, 1989. ISSN 0893-6080. doi:  
672 [https://doi.org/10.1016/0893-6080\(89\)90020-8](https://doi.org/10.1016/0893-6080(89)90020-8). URL <http://www.sciencedirect.com/science/article/pii/0893608089900208>.

674 M. Ishii and J. Tromp. Normal-mode and free-air gravity constraints on lateral variations  
675 in velocity and density of earth's mantle. *Science*, 285(5431):1231–1236, 1999. ISSN  
676 0036-8075. doi: 10.1126/science.285.5431.1231. URL <https://science.sciencemag.org/content/285/5431/1231>.

678 I. Jackson. Elasticity, composition and temperature of the Earth's lower mantle: a reap-  
679 praisal. *Geophysical Journal International*, 134(1):291–311, 07 1998. ISSN 0956-540X.  
680 doi: 10.1046/j.1365-246x.1998.00560.x. URL <https://doi.org/10.1046/j.1365-246x.1998.00560.x>.

- 682 J. M. Jackson and C. Thomas. *Seismic and Mineral Physics Constraints on the D'*  
683 *Layer*, chapter 8, pages 193–227. American Geophysical Union (AGU), 2021. ISBN  
684 9781119528609. doi: <https://doi.org/10.1002/9781119528609.ch8>. URL [https://](https://agupubs.onlinelibrary.wiley.com/doi/abs/10.1002/9781119528609.ch8)  
685 [agupubs.onlinelibrary.wiley.com/doi/abs/10.1002/9781119528609.ch8](https://agupubs.onlinelibrary.wiley.com/doi/abs/10.1002/9781119528609.ch8).
- 686 S. Jacobsen, C. Holl, K. Adams, R. Fischer, E. Martin, C. Bina, J.-F. Lin, V. Prakapenka,  
687 A. Kubo, and P. Dera. Compression of single-crystal magnesium oxide to 118 gpa and a  
688 ruby pressure gauge for helium pressure media. *American Mineralogist*, 93:1823–1828, 11  
689 2008. doi: 10.2138/am.2008.2988.
- 690 B. B. Karki, R. M. Wentzcovitch, S. de Gironcoli, and S. Baroni. First-principles determina-  
691 tion of elastic anisotropy and wave velocities of MgO at lower mantle conditions. *Science*,  
692 286(5445):1705–1707, 1999. ISSN 0036-8075. doi: 10.1126/science.286.5445.1705.
- 693 P. Käüfl, A. Valentine, R. Wit, and J. Trampert. Solving probabilistic inverse problems  
694 rapidly with prior samples. *Geophysical Journal International*, 205:ggw108, 03 2016a. doi:  
695 10.1093/gji/ggw108.
- 696 P. Käüfl, A. P. Valentine, and J. Trampert. Probabilistic point source inversion of strong-  
697 motion data in 3-d media using pattern recognition: A case study for the 2008 mw 5.4  
698 chino hills earthquake. *Geophysical Research Letters*, 43(16):8492–8498, 2016b. doi: 10.  
699 1002/2016GL069887. URL [https://agupubs.onlinelibrary.wiley.com/doi/abs/10.](https://agupubs.onlinelibrary.wiley.com/doi/abs/10.1002/2016GL069887)  
700 [1002/2016GL069887](https://agupubs.onlinelibrary.wiley.com/doi/abs/10.1002/2016GL069887).
- 701 A. Keane. An investigation of finite strain in an isotropic material subjected to hydrostatic  
702 pressure and its seismological applications. *Australian Journal of Physics*, 7:322 – 333,  
703 1954.
- 704 B. Kennett. Towards constitutive equations for the deep earth. *Physics of the Earth*  
705 *and Planetary Interiors*, 270:40 – 45, 2017. ISSN 0031-9201. doi: [https://doi.org/10.](https://doi.org/10.1016/j.pepi.2017.06.012)  
706 [1016/j.pepi.2017.06.012](https://doi.org/10.1016/j.pepi.2017.06.012). URL [http://www.sciencedirect.com/science/article/pii/](http://www.sciencedirect.com/science/article/pii/S003192011730153X)  
707 [S003192011730153X](http://www.sciencedirect.com/science/article/pii/S003192011730153X).

- 708 B. L. N. Kennett, E. R. Engdahl, and R. Buland. Constraints on seismic velocities in the  
709 earth from traveltimes. *Geophysical Journal International*, 122(1):108–124, 1995. doi: 10.  
710 1111/j.1365-246X.1995.tb03540.x. URL [https://onlinelibrary.wiley.com/doi/abs/  
711 10.1111/j.1365-246X.1995.tb03540.x](https://onlinelibrary.wiley.com/doi/abs/10.1111/j.1365-246X.1995.tb03540.x).
- 712 A. Khan, L. Boschi, and J. A. D. Connolly. On mantle chemical and thermal hetero-  
713 geneities and anisotropy as mapped by inversion of global surface wave data. *Journal*  
714 *of Geophysical Research: Solid Earth*, 114(B9), 2009. doi: 10.1029/2009JB006399. URL  
715 <https://agupubs.onlinelibrary.wiley.com/doi/abs/10.1029/2009JB006399>.
- 716 A. Khan, A. Zunino, and F. Deschamps. The thermo-chemical and physical structure beneath  
717 the north american continent from bayesian inversion of surface-wave phase velocities.  
718 *Journal of Geophysical Research: Solid Earth*, 116(B9), 2011. doi: 10.1029/2011JB008380.  
719 URL <https://agupubs.onlinelibrary.wiley.com/doi/abs/10.1029/2011JB008380>.
- 720 A. Khan, A. Zunino, and F. Deschamps. Upper mantle compositional variations and  
721 discontinuity topography imaged beneath australia from bayesian inversion of surface-  
722 wave phase velocities and thermochemical modeling. *Journal of Geophysical Research:*  
723 *Solid Earth*, 118(10):5285–5306, 2012. doi: 10.1002/jgrb.50304. URL [https://agupubs.  
724 onlinelibrary.wiley.com/doi/abs/10.1002/jgrb.50304](https://agupubs.onlinelibrary.wiley.com/doi/abs/10.1002/jgrb.50304).
- 725 A. Khan, J. A. D. Connolly, A. Pommier, and J. Noir. Geophysical evidence for melt  
726 in the deep lunar interior and implications for lunar evolution. *Journal of Geophysical*  
727 *Research: Planets*, 119(10):2197–2221, 2014. doi: 10.1002/2014JE004661. URL [https://  
728 //agupubs.onlinelibrary.wiley.com/doi/abs/10.1002/2014JE004661](https://agupubs.onlinelibrary.wiley.com/doi/abs/10.1002/2014JE004661).
- 729 A. Khan, C. Liebske, A. Rozel, A. Rivoldini, F. Nimmo, J. A. D. Connolly, A.-C. Plesa,  
730 and D. Giardini. A geophysical perspective on the bulk composition of mars. *Journal of*  
731 *Geophysical Research: Planets*, 123(2):575–611, 2018. doi: 10.1002/2017JE005371. URL  
732 <https://agupubs.onlinelibrary.wiley.com/doi/abs/10.1002/2017JE005371>.

- 733 D. P. Kingma and J. Ba. Adam: A method for stochastic optimization. *arXiv preprint*  
734 *arXiv:1412.6980*, 2014.
- 735 P. Koelemeijer, A. Deuss, and J. Ritsema. Density structure of earth's lowermost mantle  
736 from stoneley mode splitting observations. *Nature Communications*, 8:15241, 2017. doi:  
737 10.1038/ncomms15241. URL <https://doi.org/10.1038/ncomms15241>.
- 738 Y. Kono, T. Irifune, Y. Higo, T. Inoue, and A. Barnhoorn. P-V-T relation of MgO derived  
739 by simultaneous elastic wave velocity and in situ x-ray measurements: A new pressure  
740 scale for the mantle transition region. *Physics of the Earth and Planetary Interiors*, 183  
741 (1-2):196–211, 2010. doi: 10.1016/j.pepi.2010.03.010.
- 742 A. Kurnosov, H. Marquardt, D. J. Frost, T. B. Ballèvre, and L. Ziberna. Evidence for a  
743 Fe<sup>3+</sup>-rich pyrolytic lower mantle from (al,fe)-bearing bridgmanite elasticity data. *Nature*,  
744 543:543–546, 2017. doi: 10.1038/nature21390.
- 745 B. Li, K. Woody, and J. Kung. Elasticity of MgO to 11 GPa with an independent absolute  
746 pressure scale: Implications for pressure calibration. *Journal of Geophysical Research:*  
747 *Solid Earth*, 111(B11), 2006. doi: 10.1029/2005JB004251.
- 748 J.-F. Lin, S. D. Jacobsen, W. Sturhahn, J. M. Jackson, J. Zhao, and C.-S. Yoo. Sound  
749 velocities of ferropericlase in the earth's lower mantle. *Geophysical Research Letters*, 33  
750 (22), 2006. doi: 10.1029/2006GL028099. URL <https://agupubs.onlinelibrary.wiley.com/doi/abs/10.1029/2006GL028099>.
- 752 K. Litasov, E. Ohtani, A. Sano, A. Suzuki, and K. Funakoshi. In situ x-ray diffraction study of  
753 post-spinel transformation in a peridotite mantle: Implication for the 660-km discontinuity.  
754 *Earth and Planetary Science Letters*, 238(3):311 – 328, 2005. ISSN 0012-821X. doi: <https://doi.org/10.1016/j.epsl.2005.08.001>. URL <http://www.sciencedirect.com/science/article/pii/S0012821X05005236>.
- 757 L. Liu and Y. Bi. How far away are accurate equations of state determinations? some  
758 issues on pressure scales and non-hydrostaticity in diamond anvil cells. *Matter and Ra-*

- 759 *diation at Extremes*, 1(4):224 – 236, 2016. ISSN 2468-080X. doi: <https://doi.org/10.1016/j.mre.2016.06.002>. URL <http://www.sciencedirect.com/science/article/pii/S2468080X16300309>.
- 762 H. Marquardt and A. R. Thomson. Experimental elasticity of earth’s deep mantle. *Nature*  
763 *Reviews Earth & Environment*, 1:455–469, 2020. doi: 10.1038/s43017-020-0077-3. URL  
764 <https://doi.org/10.1038/s43017-020-0077-3>.
- 765 H. Marquardt, S. Speziale, H. J. Reichmann, D. J. Frost, and F. R. Schilling. Single-crystal  
766 elasticity of  $(Mg_{0.9}Fe_{0.1})O$  to 81 GPa. *Earth and Planetary Science Letters*, 287(3):345  
767 – 352, 2009. ISSN 0012-821X. doi: <https://doi.org/10.1016/j.epsl.2009.08.017>. URL  
768 <http://www.sciencedirect.com/science/article/pii/S0012821X09004889>.
- 769 H. Marquardt, J. Buchen, A. S. J. Mendez, A. Kurnosov, M. Wendt, A. Rothkirch,  
770 D. Pennicard, and H.-P. Liermann. Elastic softening of  $(Mg_{0.8}Fe_{0.2})O$  ferropericlase  
771 across the iron spin crossover measured at seismic frequencies. *Geophysical Research*  
772 *Letters*, 45(14):6862–6868, 2018. doi: <https://doi.org/10.1029/2018GL077982>. URL  
773 <https://agupubs.onlinelibrary.wiley.com/doi/abs/10.1029/2018GL077982>.
- 774 J. Matas, J. Bass, Y. Ricard, E. Matern, and M. S. T. Bukowinski. On the bulk composition  
775 of the lower mantle: predictions and limitations from generalized inversion of radial seismic  
776 profiles. *Geophysical Journal International*, 170(2):764–780, 08 2007. ISSN 0956-540X.  
777 doi: 10.1111/j.1365-246X.2007.03454.x. URL <https://doi.org/10.1111/j.1365-246X.2007.03454.x>.
- 778 2007.03454.x.
- 779 U. Meier, A. Curtis, and J. Trampert. Global crustal thickness from neural network in-  
780 version of surface wave data. *Geophysical Journal International*, 169(2):706–722, 2007a.  
781 doi: <https://doi.org/10.1111/j.1365-246X.2007.03373.x>. URL <https://onlinelibrary.wiley.com/doi/abs/10.1111/j.1365-246X.2007.03373.x>.
- 782 <https://onlinelibrary.wiley.com/doi/abs/10.1111/j.1365-246X.2007.03373.x>.
- 783 U. Meier, A. Curtis, and J. Trampert. Fully nonlinear inversion of fundamental mode surface  
784 waves for a global crustal model. *Geophysical Research Letters*, 34(16), 2007b. doi: <https://doi.org/10.1029/2007GL030000>.

785 //doi.org/10.1029/2007GL030989. URL [https://agupubs.onlinelibrary.wiley.com/](https://agupubs.onlinelibrary.wiley.com/doi/abs/10.1029/2007GL030989)  
786 [doi/abs/10.1029/2007GL030989](https://agupubs.onlinelibrary.wiley.com/doi/abs/10.1029/2007GL030989).

787 U. Meier, J. Trampert, and A. Curtis. Global variations of temperature and water con-  
788 tent in the mantle transition zone from higher mode surface waves. *Earth and Plane-*  
789 *tary Science Letters*, 282(1):91 – 101, 2009. ISSN 0012-821X. doi: [https://doi.org/10.](https://doi.org/10.1016/j.epsl.2009.03.004)  
790 [1016/j.epsl.2009.03.004](https://doi.org/10.1016/j.epsl.2009.03.004). URL [http://www.sciencedirect.com/science/article/pii/](http://www.sciencedirect.com/science/article/pii/S0012821X09001460)  
791 [S0012821X09001460](http://www.sciencedirect.com/science/article/pii/S0012821X09001460).

792 M. Murakami, Y. Ohishi, N. Hirao, and K. Hirose. Elasticity of MgO to 130 GPa: Impli-  
793 cations for lower mantle mineralogy. *Earth and Planetary Science Letters*, pages 123–129,  
794 2009. doi: [10.1016/j.epsl.2008.10.010](https://doi.org/10.1016/j.epsl.2008.10.010).

795 M. Murakami, Y. Ohishi, N. Hirao, and K. Hirose. A perovskitic lower mantle inferred  
796 from high-pressure, high-temperature sound velocity data. *Nature*, 485:90–94, 2012. doi:  
797 [10.1038/nature11004](https://doi.org/10.1038/nature11004).

798 T. Nakagawa, P. J. Tackley, F. Deschamps, and J. A. D. Connolly. Incorporating self-  
799 consistently calculated mineral physics into thermochemical mantle convection simula-  
800 tions in a 3-d spherical shell and its influence on seismic anomalies in earth’s mantle.  
801 *Geochemistry, Geophysics, Geosystems*, 10(3), 2009. doi: [10.1029/2008GC002280](https://doi.org/10.1029/2008GC002280). URL  
802 <https://agupubs.onlinelibrary.wiley.com/doi/abs/10.1029/2008GC002280>.

803 T. Nakagawa, P. J. Tackley, F. Deschamps, and J. A. Connolly. The influence of morb and  
804 harzburgite composition on thermo-chemical mantle convection in a 3-d spherical shell  
805 with self-consistently calculated mineral physics. *Earth and Planetary Science Letters*,  
806 296(3):403 – 412, 2010. ISSN 0012-821X. doi: <https://doi.org/10.1016/j.epsl.2010.05.026>.  
807 URL <http://www.sciencedirect.com/science/article/pii/S0012821X10003444>.

808 T. Nakagawa, P. J. Tackley, F. Deschamps, and J. A. D. Connolly. Radial 1-d seismic  
809 structures in the deep mantle in mantle convection simulations with self-consistently  
810 calculated mineralogy. *Geochemistry, Geophysics, Geosystems*, 13(11), 2012. doi:

- 811 10.1029/2012GC004325. URL [https://agupubs.onlinelibrary.wiley.com/doi/abs/](https://agupubs.onlinelibrary.wiley.com/doi/abs/10.1029/2012GC004325)  
812 10.1029/2012GC004325.
- 813 A. Oganov and P. I. Dorogokupets. All-electron and pseudopotential study of MgO: Equation  
814 of state, anharmonicity, and stability. *Phys. Rev. B*, 67:224110, 06 2003. doi: 10.1103/  
815 PhysRevB.67.224110.
- 816 J. Ritsema, H. J. v. Heijst, and J. H. Woodhouse. Complex shear wave velocity structure  
817 imaged beneath africa and iceland. *Science*, 286(5446):1925–1928, 1999. ISSN 0036-8075.  
818 doi: 10.1126/science.286.5446.1925. URL [https://science.sciencemag.org/content/](https://science.sciencemag.org/content/286/5446/1925)  
819 286/5446/1925.
- 820 B. Romanowicz. Using seismic waves to image earth’s internal structure. *Nature*, 451:266–  
821 268, 2008. doi: 10.1038/nature06583. URL <https://doi.org/10.1038/nature06583>.
- 822 B. S. A. Schuberth, H.-P. Bunge, G. Steinle-Neumann, C. Moder, and J. Oeser. Ther-  
823 mal versus elastic heterogeneity in high resolution mantle circulation models with py-  
824 rolite composition: High plume excess temperatures in the lowermost mantle. *Geo-*  
825 *chemistry, Geophysics, Geosystems*, 10(1), 2009. doi: 10.1029/2008GC002235. URL  
826 <https://agupubs.onlinelibrary.wiley.com/doi/abs/10.1029/2008GC002235>.
- 827 B. S. A. Schuberth, C. Zaroli, and G. Nolet. Synthetic seismograms for a synthetic Earth:  
828 long-period P- and S-wave traveltimes can be explained by temperature alone.  
829 *Geophysical Journal International*, 188(3):1393–1412, 03 2012. ISSN 0956-540X. doi: 10.  
830 1111/j.1365-246X.2011.05333.x. URL [https://doi.org/10.1111/j.1365-246X.2011.](https://doi.org/10.1111/j.1365-246X.2011.05333.x)  
831 05333.x.
- 832 M. S. Shahraeeni and A. Curtis. Fast probabilistic nonlinear petrophysical inversion. *GEO-*  
833 *PHYSICS*, 76(2):E45–E58, 2011. doi: 10.1190/1.3540628. URL [https://doi.org/10.](https://doi.org/10.1190/1.3540628)  
834 1190/1.3540628.
- 835 N. A. Simmons, A. M. Forte, L. Boschi, and S. P. Grand. Gypsum: A joint tomo-  
836 graphic model of mantle density and seismic wave speeds. *Journal of Geophysical Re-*

- 837 *search: Solid Earth*, 115(B12), 2010. doi: <https://doi.org/10.1029/2010JB007631>. URL  
838 <https://agupubs.onlinelibrary.wiley.com/doi/abs/10.1029/2010JB007631>.
- 839 S. V. Sinogeikin and J. D. Bass. Single-crystal elasticity of pyrope and MgO to 20 GPa by  
840 brillouin scattering in the diamond cell. *Physics of the Earth and Planetary Interiors*, 120  
841 (1):43 – 62, 2000. ISSN 0031-9201. doi: [https://doi.org/10.1016/S0031-9201\(00\)00143-6](https://doi.org/10.1016/S0031-9201(00)00143-6).
- 842 S. V. Sinogeikin, J. M. Jackson, B. O'Neill, J. W. Palko, and J. D. Bass. Compact  
843 high-temperature cell for brillouin scattering measurements. *Review of Scientific Instru-*  
844 *ments*, 71(1):201–206, 2000. doi: 10.1063/1.1150183. URL [https://doi.org/10.1063/](https://doi.org/10.1063/1.1150183)  
845 [1.1150183](https://doi.org/10.1063/1.1150183).
- 846 N. Solomatova, J. Jackson, W. Sturhahn, J. Wicks, J. Zhao, T. Toellner, B. Kalkan, and  
847 W. Steinhardt. Equation of state and spin crossover of (Mg,Fe)O at high pressure, with  
848 implications for explaining topographic relief at the core-mantle boundary. *American*  
849 *Mineralogist*, 101:1084–1093, 05 2016. doi: [10.2138/am-2016-5510](https://doi.org/10.2138/am-2016-5510).
- 850 S. Speziale, C.-S. Zha, T. S. Duffy, R. J. Hemley, and H.-k. Mao. Quasi-hydrostatic com-  
851 pression of magnesium oxide to 52 GPa: Implications for the pressure-volume-temperature  
852 equation of state. *Journal of Geophysical Research: Solid Earth*, 106(B1):515–528, 2001.  
853 doi: [10.1029/2000JB900313](https://doi.org/10.1029/2000JB900313).
- 854 S. Speziale, V. E. Lee, S. M. Clark, J. F. Lin, M. P. Pasternak, and R. Jeanloz. Ef-  
855 fects of fe spin transition on the elasticity of (Mg, Fe)O magnesiowüstites and impli-  
856 cations for the seismological properties of the earth's lower mantle. *Journal of Geo-*  
857 *physical Research: Solid Earth*, 112(B10), 2007. doi: [10.1029/2006JB004730](https://doi.org/10.1029/2006JB004730). URL  
858 <https://agupubs.onlinelibrary.wiley.com/doi/abs/10.1029/2006JB004730>.
- 859 F. D. Stacey. Theory of thermal and elastic properties of the lower mantle and core.  
860 *Physics of the Earth and Planetary Interiors*, 89(3):219 – 245, 1995. ISSN 0031-9201.  
861 doi: [https://doi.org/10.1016/0031-9201\(94\)03005-4](https://doi.org/10.1016/0031-9201(94)03005-4). URL [http://www.sciencedirect.](http://www.sciencedirect.com/science/article/pii/0031920194030054)  
862 [com/science/article/pii/0031920194030054](http://www.sciencedirect.com/science/article/pii/0031920194030054).

- 863 L. Stixrude and C. Lithgow-Bertelloni. Thermodynamics of mantle minerals – I. physi-  
864 cal properties. *Geophysical Journal International*, 162(2):610–632, 2005. doi: 10.1111/j.  
865 1365-246X.2005.02642.x.
- 866 L. Stixrude and C. Lithgow-Bertelloni. Thermodynamics of mantle minerals- II. phase  
867 equilibria. *Geophysical Journal International*, 184(3):1180–1213, 2011. doi: 10.1111/j.  
868 1365-246X.2010.04890.x. URL [https://onlinelibrary.wiley.com/doi/abs/10.1111/  
869 j.1365-246X.2010.04890.x](https://onlinelibrary.wiley.com/doi/abs/10.1111/j.1365-246X.2010.04890.x).
- 870 W. Sturhahn. MINeral physics UTILITY (MINUTI) open source software package, 2020. URL  
871 [www.nrixs.com](http://www.nrixs.com).
- 872 Y. Tange, Y. Nishihara, and T. Tsuchiya. Unified analyses for P-V-T equation of state  
873 of MgO: A solution for pressure-scale problems in high P-T experiments. *Journal of*  
874 *Geophysical Research: Solid Earth*, 114(B3), 2009. doi: 10.1029/2008JB005813. URL  
875 <https://agupubs.onlinelibrary.wiley.com/doi/abs/10.1029/2008JB005813>.
- 876 J. Trampert, P. Vacher, and N. Vlaar. Sensitivities of seismic velocities to tempera-  
877 ture, pressure and composition in the lower mantle. *Physics of the Earth and Plane-*  
878 *tary Interiors*, 124(3):255 – 267, 2001. ISSN 0031-9201. doi: [https://doi.org/10.1016/  
879 S0031-9201\(01\)00201-1](https://doi.org/10.1016/S0031-9201(01)00201-1). URL [http://www.sciencedirect.com/science/article/pii/  
880 S0031920101002011](http://www.sciencedirect.com/science/article/pii/S0031920101002011).
- 881 J. Trampert, F. Deschamps, J. Resovsky, and D. Yuen. Probabilistic tomography maps  
882 chemical heterogeneities throughout the lower mantle. *Science*, 306(5697):853–856, 2004.  
883 ISSN 0036-8075. doi: 10.1126/science.1101996. URL [https://science.sciencemag.  
884 org/content/306/5697/853](https://science.sciencemag.org/content/306/5697/853).
- 885 W. Utsumi, D. J. Weidner, and R. C. Liebermann. Volume measurement of MgO at high  
886 pressures and high temperatures. *Washington DC American Geophysical Union Geophys-*  
887 *ical Monograph Series*, 101:327–333, 1998. doi: 10.1029/GM101p0327.

- 888 M. S. Vassiliou and T. J. Ahrens. Hugoniot equation of state of periclase to 200 GPa.  
889 *Geophysical Research Letters*, 8(7):729–732, 1981. doi: 10.1029/GL008i007p00729.
- 890 Z. Wu, R. M. Wentzcovitch, K. Umemoto, B. Li, K. Hirose, and J.-C. Zheng. Pressure-  
891 volume-temperature relations in MgO: An ultrahigh pressure-temperature scale for plan-  
892 etary sciences applications. *Journal of Geophysical Research: Solid Earth*, 113(B6), 2008.  
893 doi: 10.1029/2007JB005275.
- 894 Y. Ye, V. Prakapenka, Y. Meng, and S.-H. Shim. Intercomparison of the gold, platinum,  
895 and MgO pressure scales up to 140 GPa and 2500 K. *Journal of Geophysical Research:*  
896 *Solid Earth*, 122(5):3450–3464, 2017.
- 897 A. Yoneda. Pressure derivatives of elastic constants of single crystal *MgO* and *MgAl<sub>2</sub>O<sub>4</sub>*.  
898 *Journal of Physics of the Earth*, 38(1):19–55, 1990. doi: 10.4294/jpe1952.38.19.
- 899 J. Zhang. Effect of pressure on the thermal expansion of MgO up to 8.2 gpa. *Physics and*  
900 *Chemistry of Minerals*, 27:145–148, 07 2000. doi: 10.1007/s002690050001.

**Declaration of interests**

The authors declare that they have no known competing financial interests or personal relationships that could have appeared to influence the work reported in this paper.

The authors declare the following financial interests/personal relationships which may be considered as potential competing interests:

Journal Pre-proof

**Author statement**

**Manuscript title:** Inferring material properties of the lower mantle minerals using Mixture Density Networks.

Ashim Rijal: methodology, software, validation, formal analysis, investigation, visualisation, writing - original draft

Laura Cobden: conceptualisation, supervision, funding acquisition, writing - review and editing

Jeannot Trampert: supervision, writing - review and editing

Jennifer M. Jackson: validation, formal analysis, writing - review and editing

Andrew Valentine: methodology, writing - review and editing